UNIVERSITY OF OKLAHOMA

GRADUATE COLLEGE

EFFECT OF OSCILLATORY SHEAR ON LATENT TGF-β ACTIVATION IN DISEASED HEART VALVES

A THESIS

SUBMITTED TO THE GRADUATE FACULTY

In partial fulfillment of the requirements for the

Degree of

MASTER of SCIENCE

By

ABIGAIL BAUKUS
Norman, Oklahoma
2021

EFFECT OF OSCILLATORY SHEAR ON LATENT TGF-β ACTIVATION IN DISEASED HEART VALVES

A THESIS APPROVED FOR THE

SCHOOL OF CHEMICAL, BIOLOGICAL, AND MATERIALS ENGINEERING

BY THE COMMITTEE CONSISTING OF

Dr. Matthias Nollert, Chair

Dr. Sepideh Razavi

Dr. Vassilios Sikavitsas

© Copyright by ABIGAIL BAUKUS 2021
All Rights Reserved.

Acknowledgements

I would like to thank my advisor, Dr. Nollert, for helping me to challenge my assumptions and grow in confidence in my skills as a graduate student. I would also like to thank Andrew D'Amico for his help in programming and validating the motor, Emad Ramadan for his assistance in helping me learn Fluent, Jasim Ahamed and the Oklahoma Medical Research Foundation for their collaboration efforts in conducting these experiments, and my committee. Finally, I would like to thank my family and friends for the immense support they have offered along this journey.

Table of Contents

Acknowledgements iv
1. Abstract viii
2. Introduction 1
2.1. The Aortic Valve and Calcific Aortic Valve Disease 1
2.1.1. Normal aortic valve anatomy and function 2
2.1.2. Disease progression 3
2.2. Shear Stress and Calcific Aortic Valve Disease 5
2.2.1. Shear-Activated Proteins 7
2.2.2. Modeling disease progression with Computational Fluid Dynamics 12
2.3. Scope of this report 15
3. Materials and Methods 16
3.1. Fluid Dynamics 16
3.1.1. Geometry and Meshing 17
3.1.2. Setting up the Solver 19
3.1.3. Validation 22
3.2. Cone and Plate Experiments 27
3.2.1. CPD setup and validation 27
3.2.2. Shear Stress Calculations 34
4. Computational Results 36
4.1. Parallel Plates 36
4.1.1. Abruptly oscillating plate 36
4.1.2. Ramped acceleration/deceleration of oscillating plate 40
4.1.3. Sinusoidally oscillating plate 43
4.1.4. Changing stop time 45
4.1.5. Reynolds number analysis 47
4.2. Cone and Plate 49
4.2.1. Shear Stress throughout cone volume 52
4.2.2 Shear Stress in the well 55
5. Discussion 57
6. Conclusions and Future Work 58
6.1. CPD Experiments 60

7. Appendices 61
7.1. Arduino Code 61
7.2. Alternative figures 67
8. References 68

Table 1: Abbreviations Used in this Thesis

Abbreviation	Meaning
CAVD	Calcific aortic valve disease
AV	Aortic valve
VECs	Valvular endothelial cells
VICs	Valvular interstitial cells
TGF-β	Transforming growth factor beta
vWF	Von Willebrand factor
CFD	Computational fluid dynamics
CPD	Cone-and-plate device

1. Abstract

Calcific aortic valve disease (CAVD) is the second leading cause of heart surgery and is responsible for about 15,000 deaths per year in North America. CAVD involves the thickening and calcification of the leaflets that comprise the aortic valve—as this occurs, the blood flow through the valve becomes disturbed and creates an environment of oscillatory pathological shear stress. The regulatory cytokine TGF-β1 is activated by shear stress and its upregulation furthers disease progression by inducing fibrosis and calcification of the cells that comprise the valve. The heart valve is difficult to study directly because of the complexity of its geometry and the heavy computational demands that modeling the valve entails. Therefore, studies have been done looking at the activation of TGF-β1 in steady vs oscillatory shear environments in a cone and plate device. In this report, the CFD software ANSYS Fluent is used to model three different oscillatory profiles in a cone and plate device: rotation of the cone with abrupt stopping, rotation with ramped acceleration/deceleration when changing directions, and sinusoidal oscillation. All three profiles generate similar time-averaged shear stresses (2.8, 2.7, 2.7 dyne/cm^2, respectively), but the abrupt stopping case generates a spike in shear stress that is nearly 50% higher than the maximum shear stresses seen in the ramped or sinusoidal cases: 14.6 vs 9.94 and 10.2 dyne/cm^2. Simulations were also run using the simpler geometry of parallel plates to validate the findings. It was found that decreasing the "stop time" when the plate's motion is abruptly stopped by an order of magnitude did not greatly affect the maximum shear stress near the plate (175 vs 169 dyne/cm^2 for stop times of 0.10 and 0.01 s, respectively), but it did result in a 3-fold increase in the ramped acceleration case: 43.2 vs 130 dyne/cm^2. These trends are independent of Reynolds number and affect about 30% of the fluid domain in the cone and plate device. Therefore, when it comes to modeling the aortic valve directly, the sensitivity of the solution to the boundary conditions depends on two

things: if the valve opening and closing occurs in a manner more similar to the abrupt or to the ramped case and the sensitivity of TGF-β1 to large spikes in shear stress.

2. Introduction

2.1. The Aortic Valve and Calcific Aortic Valve Disease

Calcific aortic valve disease (CAVD) is the most common valvular heart disease in the aging population of the developed world[1], and it is becoming increasingly prevalent and deadly. In 2019, disease prevalence was up 76% from 2010, with an age-standardized mortality rate of 1.76 per 100,000 people[2]. It is the second-highest cause of heart surgery in North America. CAVD ranges from mild thickening of the aortic valve to severe calcification. This progression begins with aortic sclerosis, which involves valve thickening without obstruction of blood flow, and ends with aortic stenosis, where the valve is severely calcified, resulting in impaired leaflet motion and left ventricular outflow obstruction[3]. This progression is shown in the figure below[4].

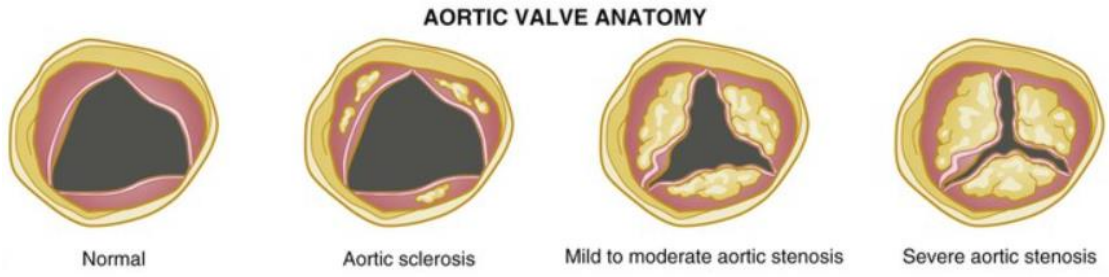

Figure 1: Progression of CAVD from a normal to severely calcified aortic valve. Image from [4].

As CAVD worsens, the valve leaflets thicken and calcium nodules form at the base of the cusps on the aortic side, gradually extending until they protrude through the orifice and interfere with the cusps' opening. The valve opening narrows, leading to increased levels of shear stress in the blood moving through the valve. Shear stress has been shown to activate molecules such as Transforming Growth Factor β (TGF-β)[5,6], which facilitate the calcification process, creating a vicious self-propagating cycle that furthers disease progression. Eventually, blood flow restriction

through the cusps leads to congestive heart failure and death[3]. Currently, the only treatment available for aortic stenosis is surgical valve replacement.

2.1.1. Normal aortic valve anatomy and function

The aortic valve (AV) lies at the junction between the left ventricle and the aorta, serving as the check valve for blood leaving the heart for systemic circulation[7]. The AV opens and closes with each heartbeat over 100,000 times a day. Because of this, as well as the significant back pressure it experiences when closed during diastole, the AV exists in a very mechanically demanding environment and must have a robust structure to guarantee its reliability[8].

The aortic valve consists of three half-moon shaped leaflets, earning it the name "semi-lunar" valve[7]. The internal framework of the leaflets consists of three distinct layers: the fibrosa, spongiosa, and ventricularis, from the aortic to the ventricular side. The fibrosa layer is closest to the outflow surface and provides most of the strength of the leaflets. It consists of dense connective tissue rich in highly aligned Type 1 collagen fibers. The central spongiosa layer is made up mainly of loose connective tissue rich in glycosaminoglycans. It provides cushioning and lubrication between the fibrosa and ventricularis. The ventricularis is closest to the inflow surface and is rich in elastin to facilitate flexibility during valve opening and closure[7].

The outside edges of the AV are lined by valvular endothelial cells, while the layered interior contains valvular interstitial cells that maintain the structural integrity of the valve leaflets[3,9].

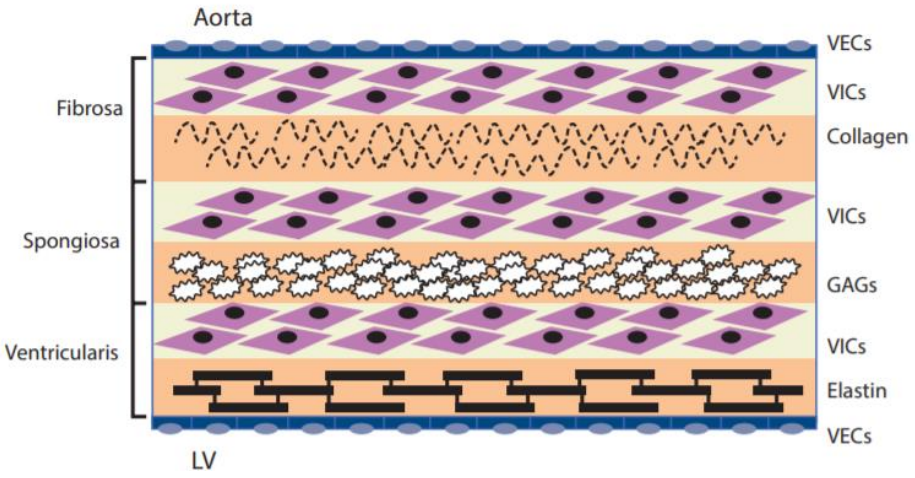

Figure 2: The layers of the aortic valve. The exteriors are lined with valvular endothelial cells (VECs), while the interior contains valvular interstitial cells (VICs). The three layers are: collagen-rich fibrosa, glycosaminoglycan (GAG)-rich spongiosa, and elastin-rich ventricularis. LV = left ventricle. Image from [3].

2.1.2. Disease progression

The classical perspective on CAVD is that this disease is degenerative (and therefore unmodifiable), wherein continued "wear and tear" on the valve over time leads to calcification and loss of function. However, evidence has shown that calcification is an actively pathobiological process, with characteristic features such as chronic inflammation, deposition of lipoproteins, and active calcification present in calcific aortic valve lesions[10].

Over recent decades, several risk factors for CAVD have been identified, many of which overlap with those of cardiovascular atherosclerosis. These include the following:

—Age	—Hypertension	—Smoking
—Male gender	—Diabetes mellitus	—Elevated cholesterol levels

In CAVD development, an initial endothelial injury triggers an inflammatory response, which leads to differentiation of VICs into myofibroblasts and osteoblasts and subsequent calcification[11]. Mechanical and shear stresses combined with the given risk factors create an initial endothelial injury, causing an inflammatory response in the tissue. This inflammatory response is

characterized by the deposition of oxidized low-density lipoproteins and the presence of cell types commonly associated with chronic inflammation, such as macrophages and T-lymphocytes. Within the lesion, the valvular interstitial cells begin to differentiate into myofibroblasts and osteoblasts, a process mediated in part by inflammatory cytokines such as transforming growth factor beta (TGF-β), tumor necrosis factor (TNF)-α, and interleukin-1β. These differentiated VICs are then responsible for the active deposition of calcium during CAVD[3]. Proteins such as bone morphogenic proteins (BMP-2 and -4) and receptor activator of nuclear factor NF-κB ligand (RANKL) have been detected in calcified tissue and are involved in tissue calcification regulation[11].

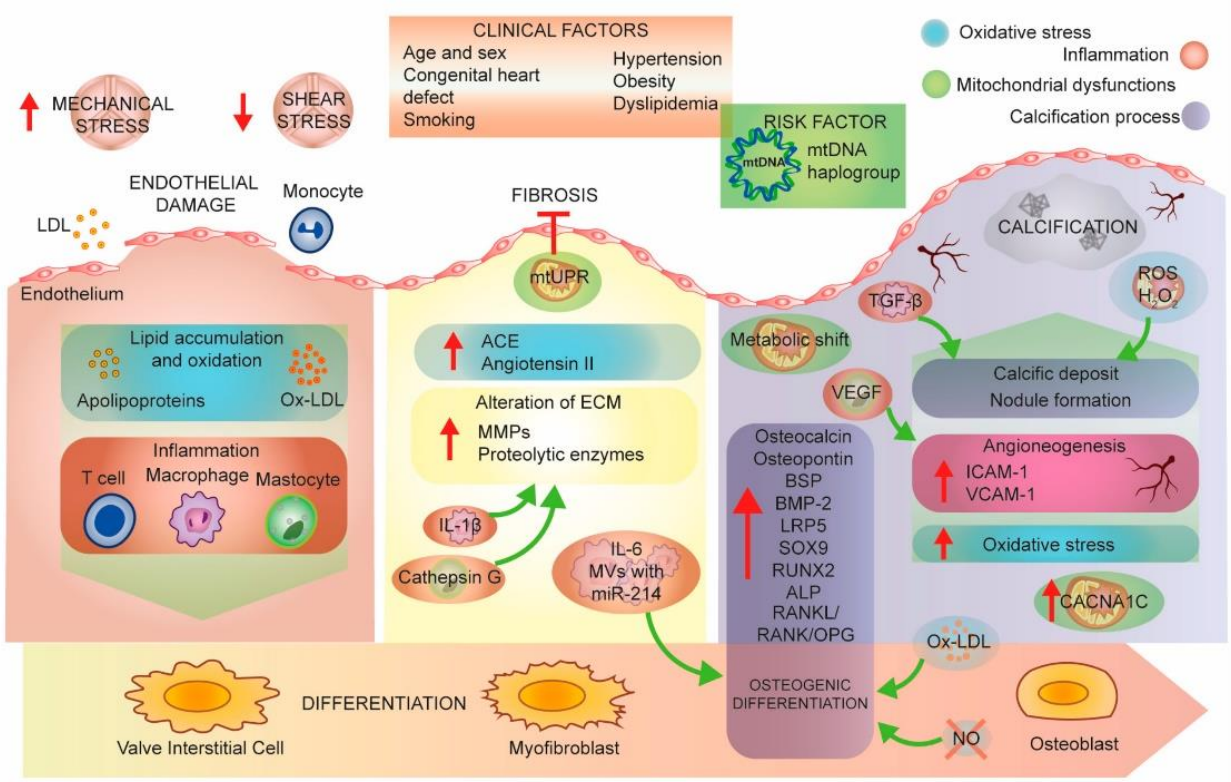

Figure 3: Aortic stenosis pathobiology. An initial endothelial injury triggers an inflammatory response, which leads to differentiation of VICs into myofibroblasts and osteoblasts and subsequent calcification. Image from [11].

Table 2: Figure 3 Abbreviations

LDL	Low-density lipoprotein	RUNX2	runt-related transcription factor 2
oxLDL	oxidized LDL	ALP	alkaline phosphatase
mtUPR	mitochondrial unfolded protein response	RANKL	receptor activator of NF-kappa B ligand
ACE	angiotensin-converting enzyme	RANK	receptor activator of nuclear factor κ
		OPG	osteoprotegerin
ECM	extracellular matrix	NO	nitric oxide
MMPs	matrix metalloproteinases	VEGF	vascular endothelial growth factor
MVs	microvesicles	TGF-β	transforming growth factor beta
TNF-α	tumor necrosis factor α	ROS	reactive oxygen species
BSP	bone sialoprotein	ICAM-1	intercellular adhesion molecule 1
BMP-2	bone morphogenetic protein	vCAM-1	vascular cell adhesion molecule 1
LRP5	LDL receptor-related protein 5	CACNA1C	calcium voltage-gated channel subunit alpha 1 C
SOX9	SRY-box 9		

In sum, CAVD is an active pathobiological process where the aortic valve becomes inflamed, leading to osteoblastic transformation and bone formation, which eventually inhibits valve leaflet motion, restricts blood flow, and causes death.

2.2. Shear Stress and Calcific Aortic Valve Disease

Shear stress arises from a tangential force (such as a flowing fluid) acting on a surface. Its units match that of pressure: force per unit area, often expressed in Pa or dyne/cm^2 (1 Pa = 10 dyne/cm^2). It is calculated as the gradient of the velocity (shear rate) multiplied by the viscosity of the fluid. The equation below describes the shear stress for one component using Newton's Law of Viscosity[12]:

$$\tau_{xy} = \mu * \frac{dv_x}{dy} \qquad \textit{Equation 1}$$

While blood is a non-Newtonian fluid, it follows Newtonian behavior for shear rates > 100 s^{-1}. The effect of non-Newtonian behavior in flow is not significant in large blood vessels such as the aorta, where shear rates are high[13]. Therefore, the often-used approximation of blood as a Newtonian fluid will be applied in this thesis, with fluid properties matching that of water.

In the body, the endothelium that lines the cardiovascular system is highly sensitive to the shear stresses that act on the vessel walls in the direction of flow. Physiological shear stress has been shown to be critical to the maintenance of normal vascular function and homeostasis. Conversely, shear stress that arises from "disturbed" (i.e. nonlaminar, or otherwise pathological) flow plays a role in the pathogenesis of atherosclerotic plaque[14].

The vascular and valvular endothelium play important roles in mediating hemodynamic and humoral stimuli. In non-pathological conditions, fluid shear stress has been shown to promote anti-inflammatory and anti-oxidizing gene expression[15]. This "good" shear stress is characterized by steady, unidirectional, laminar flow. It results in upregulation of antioxidants such as CYP1A1, PRDX1, and SOD2, and downregulation of proinflammatory mediators such as BMP-4 and CAD11, which induce differentiation of cells into chondrogenic (cartilage forming) and osteogenic (bone forming) phenotypes[16].

There are several reasons to suggest that altered flow patterns may contribute causally to the initiation of valvular pathogenesis. To begin with, several studies have shown that endothelial inflammation and atherosclerosis occur preferentially at sites of low or oscillatory flow (often characterized in literature as "disturbed" flow)[17]. Additionally, most calcific lesions form on the aortic rather than ventricular side of the AV. The aortic surface experiences a more complex circulating flow that differs from the unidirectional flow on the leaflet's ventricular side[18], suggesting that it is this difference in flow that affects the development of the calcific lesions characteristic of CAVD. An analysis of gene expression profiles on each side of the AV showed that while the aortic side is protected in normal conditions against inflammation and lesion initiation, it is also "permissive to calcification" in a way that the ventricular side is not[15].

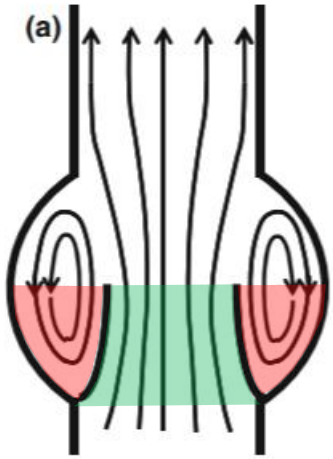

Figure 4: Shear stress acting on the aortic valve. The ventricular side of the valve (green) experiences more steady, unidirectional flow while the aortic side (red) experiences more oscillatory flow. Image adapted from [15].

It is worth investigating the effect that shear stress arising from "disturbed" flow has on the initiation and progression of CAVD. The aortic side of the AV expresses elevated levels of cell adhesion molecules and markers of inflammation when exposed to non-physiologic shear stress. Altered shear stress causes TGF-β1 expression, which in turn causes BMP-4 expression. This BMP-4 expression results in increased inflammatory responses, as confirmed by increases in the leukocyte adhesion molecules ICAM-1 and VCAM-1[19]. It is worth noting that the activated TGF-β comes primarily from platelets circulating in the blood, so while the endothelial response to shear is important, the focus of this report is on how TGF-β in the blood activates and contributes to the progression of CAVD.

2.2.1. Shear-Activated Proteins

2.2.1.1. The von Willebrand Factor (vWF)

TGF-β is not the first shear-activated soluble protein to be discovered. Other proteins in the body have been found to respond to mechanical stimuli such as shear stress. The best-studied example of a shear stress-mediated protein is that of the von Willebrand factor (vWF)[20]. vWF is a

large glycoprotein that plays a key role in the formation of blood clots. Blood clot formation is a complex process that involves platelet aggregation and adherence at the site of injury, which requires binding between multiple receptor-ligand pairs. vWF facilitates platelet adhesion through its binding to molecules such as Factor VIII, collagen, and platelet GPlb (glycoprotein lb)[21].

vWF is normally present in the blood in a loosely coiled, globular structure. However, when exposed to shear rates greater than 1000 s^{-1}, the molecule abruptly changes its conformation, elongating until linear. This exposes the A1 domain on the protein, which is the binding site for platelet GPlb. When shear rates get above 5000 s^{-1}, the A1 domain is activated and experiences a much higher binding affinity for GPlb[22]. Shear rates this high are pathological and can be found at sites of vascular injury where vasoconstriction reduces the blood vessel diameter.

The elongation of vWF and subsequent activation of the A1 domain is easily reversible—vWF will return to its globular state as soon as the flow returns to normal, for example downstream of the site of an injury[23].

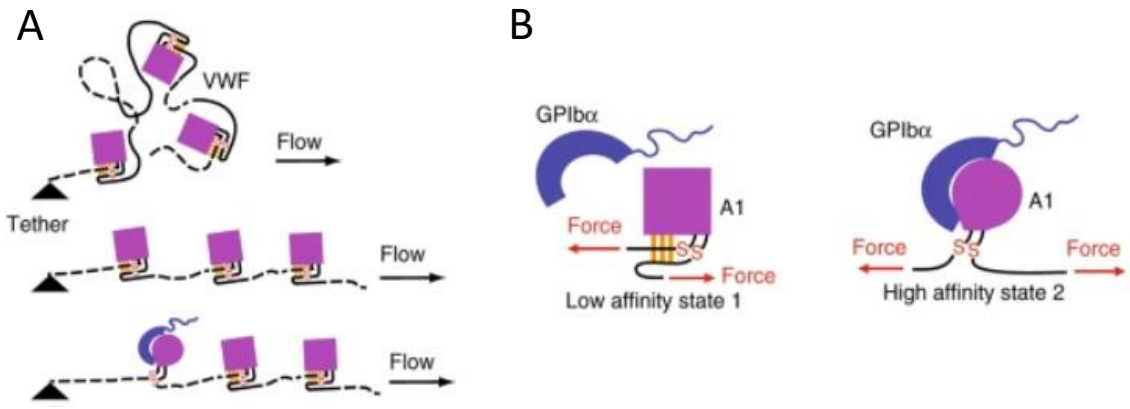

Figure 5: Mechanical activation of vWF. A) vWF, tethered to the endothelium, is elongated and activated by high levels of shear stress. B) Schematic showing the activation of the A1 domain of vWF, where it has a high affinity for the platelet GPlbα. Image from [23].

The flow-mediated activation of vWF is integral to the immune response. It prevents the buildup of platelets under normal physiological conditions and preserves homeostasis by

facilitating clot formation should an injury occur in the vasculature. Areas of high shear are more susceptible to injury, so having shear increase the binding probability of vWF serves as an effective self-regulating repair mechanism[24].

While not relevant to the conversation about CAVD, vWF is an important example of how shear stress can play a major role in protein activation.

2.2.1.2. Transforming Growth Factor Beta (TGF-β)

Transforming growth factor beta, or TGF-β, is a regulatory cytokine that plays a role in immune response suppression, cell differentiation, and tissue repair[25]. It is part of the TGF-β superfamily, which is a large group of proteins that includes the activin/inhibin family, bone morphogenic proteins (BMPs), growth differentiation factors (GDFs), and the glial cell line-derived neurotropic factor (GDNF) family[26]. The TGF-β superfamily is important for regulating a variety of biological processes such as cell growth, development, tissue homeostasis, and immune system regulation.

The TGF-β subfamily consists of homodimeric polypeptides that have multiple regulatory properties. Peptide secretion is both temporal and tissue-specific, allowing for integration of multiple cell types and pathways. TGF-β has been found in three isoforms: types I, II, and III. TGF-β1 is the most abundant and ubiquitously expressed and will be the focus moving forward.

TGF-β has been found in almost all cell types, but is most prevalent in platelets, which are responsible for ~45% of the latent TGF-β in circulation and have 40-100x more TGF-β than other cell types[27]. It is produced in a latent form and then binds to its receptors when activated, which triggers a host of signaling cascades.

Latent TGF-β consists of the molecule noncovalently bound to its precursor, called latency-associated peptide (LAP). The LAP is disulfide bonded to a latent TGF-β binding peptide (LTBP),

which plays an important role in tying TGF-β to the extracellular matrix. This complex is known as the large latent complex (LLC)[25,27].

Latent TGF-β cannot bind to its receptors until it is activated. Activation consists of freeing the TGF-β molecule from the LAP by an activator (TA). This activation has been shown to be mediated by shear stress[6,27,28,29,30]. Little is known about the specifics of how shear stress activates TGF-β, but studies have found potential mechanisms to be modulation by potassium ion channel currents[6] and by thiol-disulfide exchange[27].

Once activated, the TGF-β dimer binds to TGF-β receptor II, which recruits TGF-β receptor I (also known as ALK5), forming a heterodimeric complex. These receptors are serine/threonine kinases[25]. This phosphorylates the receptors' intracellular kinase domains, activating them. The active kinase domains can then phosphorylate SMAD transcription factors. The phosphorylation of the SMAD transcription factors make up TGF-β's canonical signaling pathway. SMADs 2 and 3 are phosphorylated by the activated kinase domains and form a heterotrimeric complex with the co-factor SMAD 4. This complex enters the nucleus and acts on the TGF-β target genes. This canonical TGF-β signaling pathway is shown in Figure 6, below[31].

TGF-β can also act through non-canonical signaling pathways. These include the MAPK pathway (which involves ERK1/ERK2, JNK, p38, and PI3K kinases), Notch signaling, AKT/PKB, GTP-binding proteins pathway, PTK, NF-κB, and Wntβ-catenin. This allows TGF-β to indirectly participate in cell apoptosis, endothelial-to-mesenchymal transition, cellular migration, proliferation, differentiation, and matrix formation.

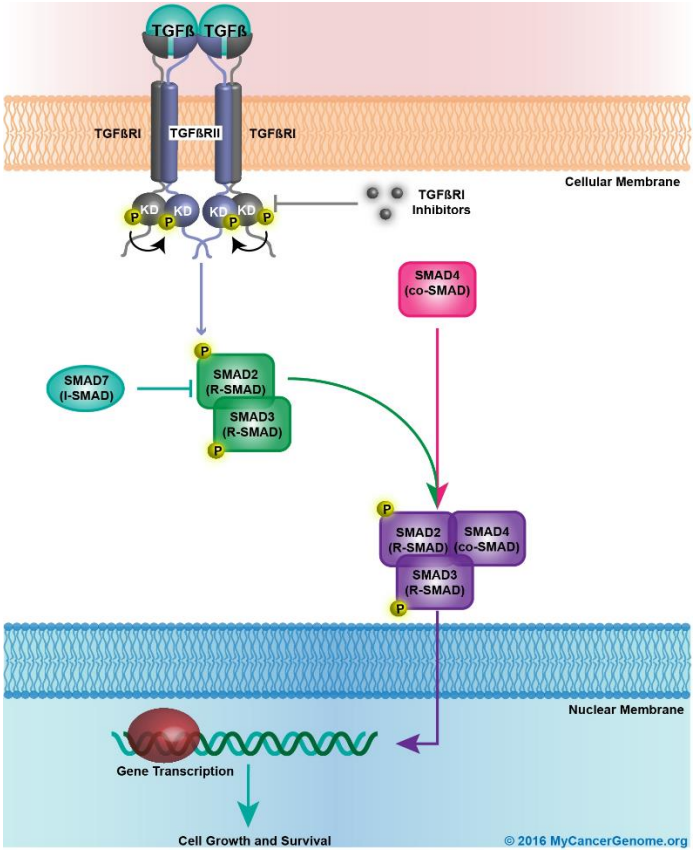

Figure 6: TGF-Beta canonical cell signaling pathway. Activated TGF-β binds to its receptors, activating their intracellular kinase domains (KD). This leads to the phosphorylation of SMADs 2 and 3, which, in conjunction with co-factor SMAD 4, form a complex that enters the nucleus and triggers gene transcription. This process could be blocked by TGF-β receptor or SMAD inhibitors. Image from [31].

Upregulation of TGF-β signaling has been heavily implicated in the progression of CAVD, as it induces fibrosis and calcification[32,33]. TGF-β triggers the transformation of VICs into collagen-producing myofibroblasts though its canonical (SMAD) signaling pathway[34]. Additionally, TGF-β mediates the calcification of valves via apoptotic mechanisms[33].

TGF-β activation increases with increasing shear stress[27,29]. As aortic valve stenosis worsens, the valve opening narrows, leading to increased levels of shear stress. This increase in shear stress increases TGF-β activation, which increases calcification, creating a vicious self-propagating cycle. Therefore, understanding TGF-β's sensitivity to shear stress could be crucial in developing treatments for CAVD.

2.2.2. Modeling disease progression with Computational Fluid Dynamics

Computational fluid dynamics (CFD) has emerged in recent years as a powerful tool in system design and optimization within industries such as chemicals, aerospace, and hydrodynamics. It is also used to increase understanding of the biomechanical behavior of blood flow in normal and pathological blood vessels. The impact of CFD has only increased as technological advances are made in computing power, coupled with cost reductions in the equipment needed for supercomputing[35].

CFD modeling is becoming increasingly important in the field of cardiovascular medicine. It can enhance diagnostic assessment, device design, and aid in clinical trials by contributing to our understanding of the physiological responses to intervention and by computing unmeasurable hemodynamic parameters[36]. For example, patient-specific modeling can be used to determine whether surgical intervention is needed in cerebral aneurisms by assessing the rupture risk due to altered hemodynamics[37,38]. CFD modeling has also been used to simulate transcatheter aortic valve degeneration[39] and more broadly in modeling the hemodynamic parameters of diseased aortas[35,40]. In sum, CFD modeling has immense potential in the field of cardiovascular medicine for both clinical and research applications—improving treatments and developing new ones.

However, it is important to understand the current limitations CFD modeling faces, particularly in the field of cardiovascular medicine. CFD modeling is difficult—complications arise from meshing the solid-fluid boundary, modeling the coupled fluid-solid interaction, modeling transitional flow, turbulence, and reaching Reynolds numbers of peak flow at physiological levels[41]. Fluid-structure interactions (FSI) play a major role in modeling blood flow correctly—blood vessels and valves change dynamically with changes in pressure and velocity, and this changing geometry must be accounted for. For example, in the case of the cerebral

aneurisms given above, FSI models produce lower values of wall shear stress than rigid-wall models, which could be the difference between an invasive surgery needing to be performed and not[42]. In the aortic valve, FSI is complicated to model because of the large motion of very thin leaflets through the fluid domain. Progress is being made[43,44], but a complete, robust FSI model of the aortic valve has yet to be developed.

Despite its limitations, CFD modeling of the aortic valve is still crucial to understanding the changing hemodynamics associated with CAVD. Valve modeling begins with clinical imaging of the area, using technologies such as ultrasound, CT, MRI, and X-ray angiography. From there, the images are converted into geometries with clearly defined physical boundaries in a segmentation and reconstruction step. Then, the geometry can be discretized (meshed), boundary conditions established, and solution methods applied[36]. The accuracy of the solution is therefore heavily reliant on precise imaging technology.

CFD modeling of the aortic valve has been used to estimate valvular resistance[45], abnormalities in the wall shear stresses of bicuspid aortic valves[46], and other hemodynamic properties in the aorta[35,47].

2.2.2.1. Testing with a Cone and Plate Device

Because of the challenges of modeling the human aortic valve directly, some researchers have turned to using simpler geometries and idealized flows in studying the mechanobiology of the aortic valve[41]. Typical simplification approaches include building geometries with rigid walls and using steady flows. These simpler geometries are also useful in connecting computational models to *ex vivo* experiments. The cone and plate device (CPD) is one such example—it is used to mimic the flows of the arterial system on endothelial cells *ex vivo.* The advantage to the cone and plate device is that it produces a nearly uniform shear stress environment and allows wider

ranges of flow regimes and shear stresses with a lower volume of fluid than parallel plate apparatuses[48].

The CPD consists of an inverted cone that rotates just above a flat stationary plate. Fluid fills the well between the cone and plate and tissue samples can placed on the surface of the plate. Fluid shear stresses are generated by rotating the cone at different angular velocities[49].

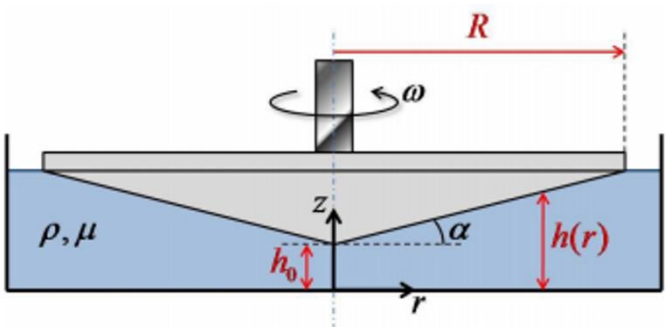

Figure 7: General schematic of a cone and plate device. The device consists of a cone with radius R and angle α placed at a height h_0 above a flat plate, creating a well that is filled with fluid. The cone rotates with angular velocity ω, subjecting the fluid in the well to shear stresses. Image from [49].

Sucosky *et al.* built a cone and plate device designed to expose whole tissue samples to physiological shear stress while minimizing radial secondary flows, which can occur at higher Reynolds numbers or if the cone angle or gap between the cone and plate are too large[48]. Kouzbari *et al.* used a CPD to demonstrate that oscillatory shear potentiates the activation of latent TGF-β more than steady shear, by measuring the amount of active TGF-β in platelet releasates after exposure to the shear stress generated by constant rotation of the cone and by rotation of the cone with abrupt changes in direction[50]. It has also been shown that the time lag between the cone rotation and shear stress generated on the plate is negligible (on the order of 10^{-3} s)[51], which suggests that the system can apply both temporally unsteady and spatially non-uniform flow[52].

In sum, the CPD is a useful apparatus that can expose endothelial cells or fluids to different shear stress profiles to enhance understanding of how shear stresses regulate the severity of

cardiovascular diseases. It is necessary to use computational simulation to fully elicit the details of the flow that is imposed in these devices[51]. However, these simulations typically focus on the shear stresses on the plate, where tissue samples are placed[53]. Here, we are interested in the activation of TGF-β in the blood, so the shear stresses throughout the entire fluid domain in the CPD are important. Combining the experimental and computational approaches will be critical to further understanding the progression of atherosclerotic and stenotic diseases as they relate to fluid flow.

2.3. Scope of this report

In this report, CFD analysis is run to understand the shear stress profiles generated by different types of oscillatory shear in two different geometries—semi-infinite parallel plates and a cone and plate device. Validation is shown for a cone and plate device programmed to generate three different oscillatory shear stress profiles and section 6.1 outlines the experimental procedure for using the device to test the effect of the shear profiles on the activation of latent TGF-β in platelet releasates. Note: the original intent was that these experiments would be performed in conjunction with the CFD analysis, but they were not able to be carried out because of COVID-19 restrictions.

Through modeling the different oscillatory profiles, we can see how sensitive these time-dependent flow fields are to subtle changes in the boundary conditions. If the shear stresses in the fluid only change slightly with changes in the motion of the cone (CPD geometry) or plate (parallel plate geometry), then the boundary conditions do not need to be modeled as precisely as if small changes in wall motion generate large changes in shear stress. These limits on how precisely we need to know the wall motion to estimate the bulk shear stresses in the fluid will be important to future computational and imaging studies.

Additionally, most of the literature investigating the activation of latent TGF-β has studied the effect of no shear vs shear, or constant shear vs oscillatory shear. Little is known about the exact mechanism of activation. By analyzing different types of oscillatory shear, we will be able to elicit more information about how latent TGF-β is activated—does the activation come from transient spikes in shear stress, or does it come from spending time at a certain elevated level of shear? A better understanding of the mechanisms of TGF-β and how it relates to shear stress near the aortic valve has clinical implications for disease treatment and will contribute to future modeling and studies of TGF-β and shear stress.

3. Materials and Methods

3.1. Fluid Dynamics

The computational software package used in this thesis is ANSYS Fluent[54]. Fluent works by solving the governing integral equations for the conservation of mass and momentum. It utilizes a control-volume based technique that involves dividing the domain into discrete control volumes, integrating the governing equations on the control volumes, constructing algebraic equations to solve for unknowns such as velocity, temperature, and pressure, and linearizing the discretized equations and solutions to yield updated values of the unknowns[54]. This allows one to get solutions to problems in fluid dynamics that cannot be solved analytically, such as those with several velocity components that are functions of several variables[12].

There are four primary steps to running a simulation in Fluent: building the geometry, meshing the geometry, setting up the solver, and postprocessing. The geometry is built using Design Modeler, where two-dimensional sketches can be extruded or rotated to yield three-dimensional bodies with specified dimensions. The bodies are then meshed to create the

computational grid of discrete control volumes. The quality of mesh plays a significant role in the accuracy and stability of the simulation and is based on factors including node point distribution, smoothness, and skewness[54]. A solution method is then chosen while setting up the solver and parameters such as inputs and boundary conditions are specified. Finally, during postprocessing, one can analyze the results of the computation.

Two different geometries were used in this report: semi-infinite parallel plates and a cone-and-plate device (CPD). The cone and plate geometry matches that of devices used in laboratory experiments[50]. The parallel plate geometry is simpler and is used to validate that Fluent is being used correctly, as well as to serve as a check that the cone and plate results make sense. Aortic valves were not modeled directly for several reasons. While studies have been done to simulate flow in heart valves[18,36,39], the fact remains that numerically modeling the aortic valve is difficult. Complications arise from meshing the solid-fluid boundary, modeling the coupled fluid-solid interaction, modeling transitional flow, turbulence, and reaching Reynolds numbers of peak flow at physiological levels[41] (see 2.2.2 for a more detailed explanation of the limitations of modeling aortic valve flows). Therefore, the simplified geometry of the CPD case will be used to model different velocity profiles.

3.1.1. Geometry and Meshing

To construct the parallel plates, a two-dimensional rectangular sketch (in the XY plane) was built in the geometry Design Modeler. The sketch was then extruded in the Z direction to become three-dimensional. The geometry was then meshed using the Fluent Mesh-Modeler, with the following parameters:

Aspect Ratio: Min = 1.0101, Max = 1.0110, Average = 1.0101

Orthogonal Quality: Min = 1.000, Max = 1.000, Average = 1.000

Skewness: Min = 1.3E-10, Max = 5.0E-04, Average = 9.0E-06

The aspect ratio is a measure of the stretching of a cell, calculated as the ratio of the maximum and minimum values of the distances between cell and face centroids, or cell centroids and nodes. The orthogonal quality relates to how closely angles between adjacent element edges are to an optimal angle. The skewness is the difference between the cell's shape and the shape of an equilateral cell of equivalent volume—the lower the skewness, the more accurate and stable the solution. The following figure shows the meshed geometry of the parallel plates.

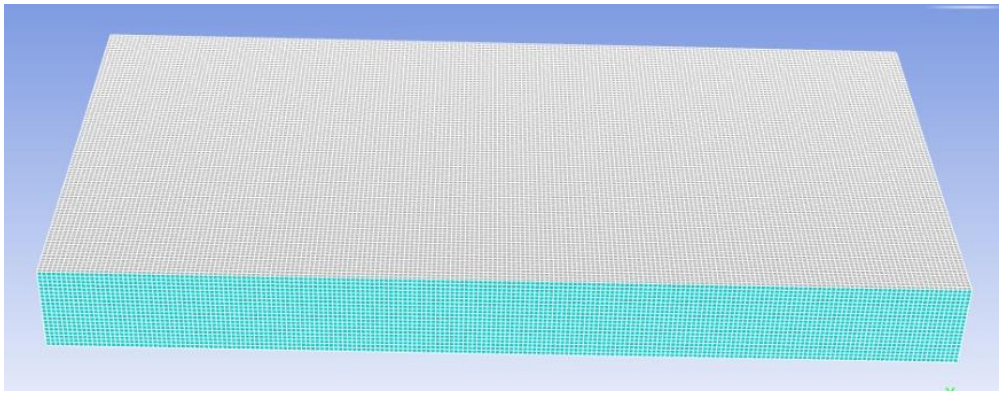

Figure 8: Parallel plate meshed geometry

To construct the cone and plate device, a two-dimensional sketch was built in Design Modeler and then rotated around the Y axis to become three-dimensional. The meshed geometry had the following properties:

Aspect Ratio: Min = 1.1575, Max = 9.5065, Average = 1.8781

Orthogonal Quality: Min = 0.2013, Max = 0.9948, Average = 0.7567

Skewness: Min = 5.4E-09, Max = 0.7987, Average = 0.2414

Note: A general rule for triangular/tetrahedral mesh (as is used here) is a skewness with a maximum below 0.95 and an average below 0.33[54]. The following figure shows the meshed geometry of the cone and plate:

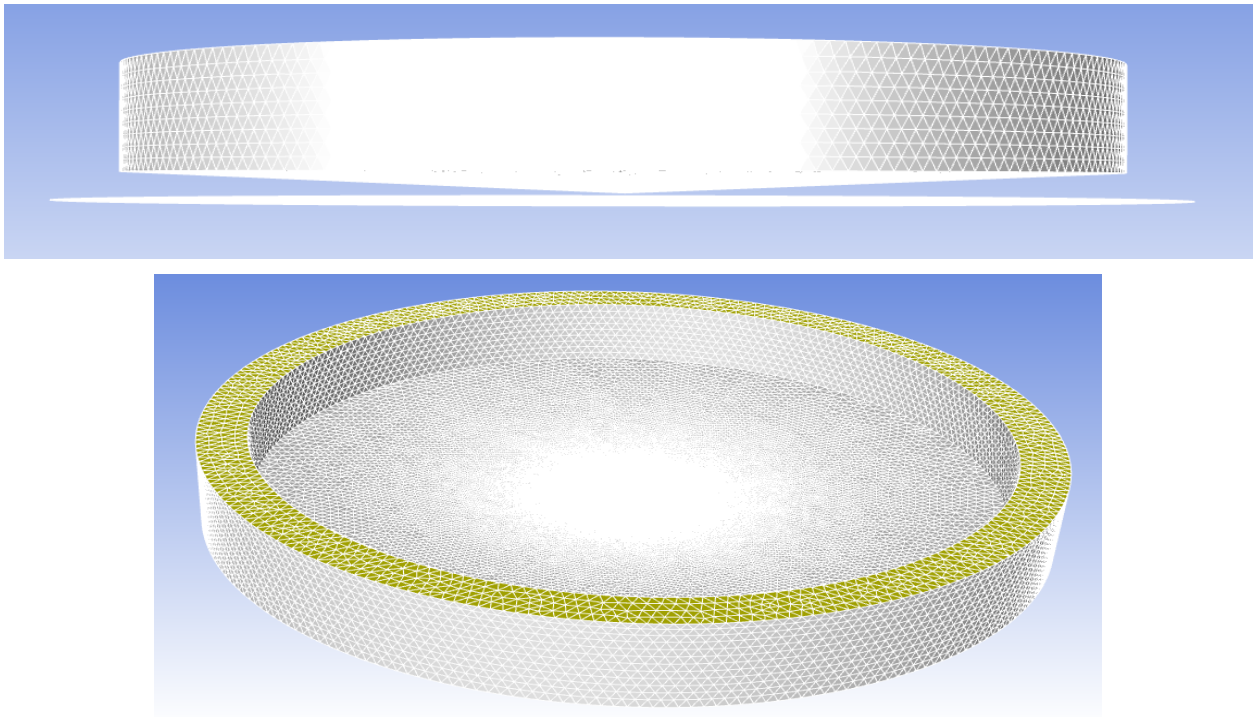

Figure 9: Cone and plate meshed geometry. Side and top views shown.

3.1.2. Setting up the Solver

The solver used is pressure-based, with absolute velocity formulation (as opposed to relative), with either steady or transient time, depending on the case. The solution methods are SIMPLE scheme pressure-velocity coupling, with spatial discretization as follows: Least Squares Cell-Based Gradient, Second Order Pressure, and Second Order Upwind Momentum. In transient cases, the formulation was First Order Implicit. The cases were initialized using hybrid initialization because there were no inlets or outlets in the system.

In all cases, the material chosen was water, with constant density = 998.2 kg/m^3 and viscosity = 0.001003 kg/m/s.

The boundary conditions were as follows:

Table 3: Parallel Plate Boundary Conditions

Zone	Boundary Condition
Interior	Interior-solid
Top Plate (Y = 1 mm)	Moving Wall: Absolute translational motion, no slip shear
Bottom Plate (Y = 0 mm)	Stationary Wall: no slip shear
XZ Plane	Periodic: Translational

The periodic boundary condition works to essentially make the plates unbounded in the XZ plane, so that edge effects do not need to be considered and the flow is fully developed. In all cases, the plate's motion is in the X-direction, making that the only nonzero component of the fluid velocity, with a velocity gradient in the Y-direction (the gap between the two plates). The operating pressure is set to 101325 Pa and the periodic pressure gradient is set to 0 Pa/m unless otherwise specified.

Table 4: Cone and Plate Boundary Conditions

Zone	Boundary Condition
Free Surface	Symmetry Wall
Cone	Moving Wall: Absolute rotational motion (Y axis), no slip shear
Plate	Stationary Wall: no slip shear
Side Wall	Stationary Wall: no slip shear

The cone rotates around the Y-axis (the Θ- direction), creating velocity gradients in multiple directions: vertically, between the cone and plate (along the Y-axis), and outwards in the radial direction (the XZ plane in Cartesian coordinates).

The boundary conditions for moving walls were set in one of two ways: a User-Defined Function (UDF), or a profile. The UDF involves writing the boundary condition as a function, using the programming language C. It was used to create sinusoidally oscillating motion, as the wall velocity is a continuous function of time. A profile allows the user to input specific time and velocity (or other relevant parameters) coordinates, that Fluent can then read and execute as the run progresses. This is particularly useful for creating boundary conditions that are step-wise

functions, which are difficult to write as a UDF. Profiles were used for the oscillatory cases that involved abrupt stops and ramped acceleration.

The Solver was then programmed to run for a specified number of time steps at a given time step-size, with a set number of iterations per time step. The time step chosen needs to be small enough that the solution converges accurately and is stable, without taking too much computation time. A time-step independence analysis was performed to check the largest time-step that could be used without sacrificing accuracy:

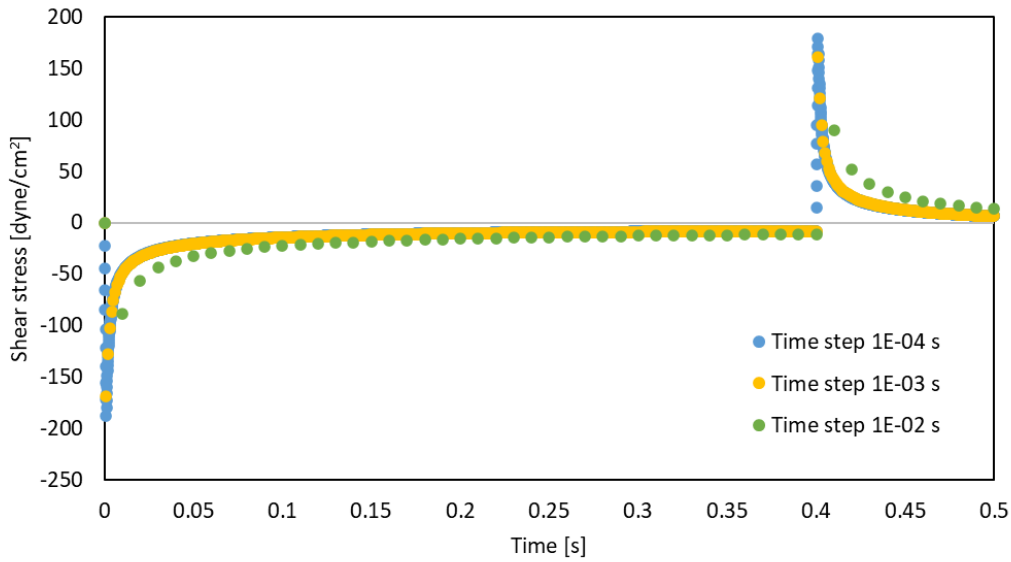

Figure 10: Time-step independence analysis. Calculated shear stress on the surface of a parallel plate moving at 1 m/s for 0.4 seconds in one direction, before stopping abruptly for 0.1 seconds.

The largest difference in calculated shear stress between the different time steps was seen at the point of maximum shear stress. The difference in maximum values for the 1E-03 and 1E-04 second time steps were within 10%, with an average difference in shear stress of 2.7%. These differences were deemed small enough that a 1E-03 second step size was acceptable and was the step size used in all runs moving forward.

3.1.3. Validation

To confirm the accuracy of the set-up in Fluent, several cases were run that have known analytical solutions. The computational and analytical solutions were compared to ensure that the computational solutions generated by Fluent were in good agreement with the calculated analytical results. Validation was run for both steady and transient flow in the parallel-plate geometry and steady flow with the cone-and-plate geometry.

3.1.3.1. Parallel Plate

3.1.3.1.1. Steady state

Flow between parallel plates is a case that has been extensively studied in fluid dynamics because its simple geometry allows for robust analytical solutions. The simplest case is that of pressure-driven flow between two semi-infinite stationary plates. Using the coordinate system established in 3.1.1, the fluid is moving only in the X-direction and is a function of only one independent variable: position in the Y-direction, which is the vertical distance between the two plates. The fluid has the following velocity profile, at steady-state and ignoring end effects[55]:

$$v_x(y) = \frac{1}{2\mu}\left(\frac{dP}{dx}\right)[y^2 - Ly] + \frac{v_0 y}{L} \qquad \textit{Equation 2}$$

where μ is the viscosity of the fluid in [Pa*s], dP/dx is the imposed pressure drop in [Pa/m], L is the distance between the two plates in [m], and v_0 is the velocity of one of the plates in [m/s], equal to 0 in the case that both plates are stationary.

A simulation was conducted in Fluent with the following conditions: Both plates stationary, an imposed pressure gradient of 1000 Pa/m, using the steady-state solver for 1000 iterations. The results from the simulation are compared to the analytical solution in the figure below:

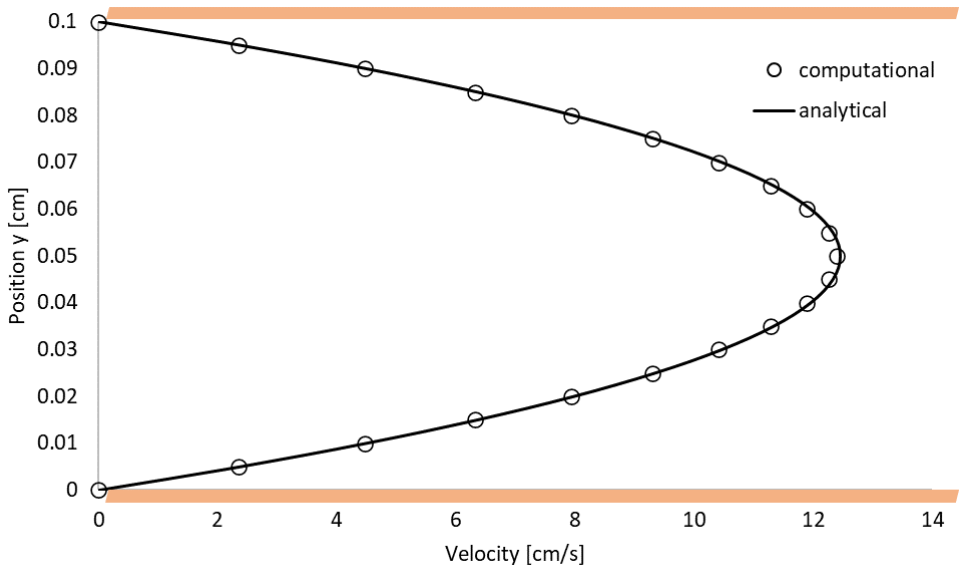

Figure 11: Pressure-driven flow between two stationary parallel plates. The analytical solution (solid line) is calculated from Equation 2, with a plate distance of 0.1 cm and a pressure drop of 1000 Pa/m. The orange bars visually represent the stationary plates.

To further validate this solution, the solver was run again, only this time, the boundary condition of the top plate was set to a constant -10 cm/s, making the final term in Equation 2 nonzero (v_0 = -0.1 m/s). The computational and analytical results for this case are shown below.

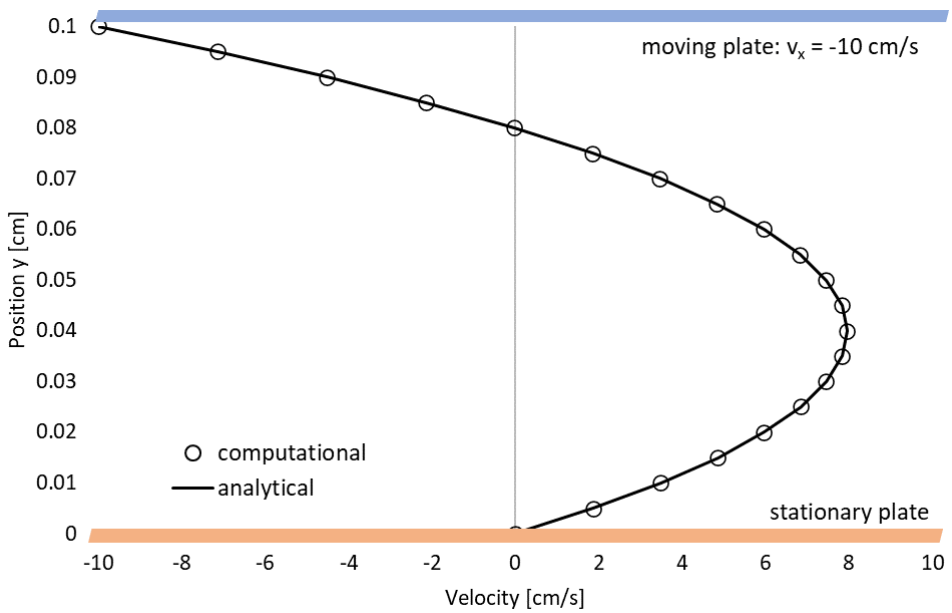

Figure 12: Pressure-driven flow between two parallel plates. The solid line is calculated from Equation 2, with a plate distance of 0.1 cm, a pressure drop of 1000 Pa/m, and a top plate velocity of -10 cm/s. The orange bar represents the stationary plate, and the blue bar represents the moving plate.

As can be seen from these figures, the computational solution gives good agreement with the analytical solution in this simple case of pressure-driven flow between parallel plates.

3.1.3.1.2. Transient

Parallel plate problems can quickly grow in complexity as independent variables are added. For example, the analytical solution to flow between parallel plates with one plate moving and no pressure drop is a simple linear function. That case, however, becomes much more complicated when considering its startup (from the time the plate is set in motion to the time it reaches steady state). Before the fluid motion reaches steady-state, it is a function of two independent variables: position (in the Y-direction) and time t.

The analytical solution to this case involves an infinite series. It consists of a steady-state term minus a transient term that fades out with increasing time, until the solution converges with the steady-state case (Equation 2).

This solution is more conveniently calculated with dimensionless rather than absolute variables. Use of dimensionless variables offers several advantages—the final solution ends up independent of specific geometric parameters, units do not need to be kept consistent throughout the calculation, and it allows one to reduce partial differential equations that are functions of multiple variables down to functions of single variables. The relevant dimensionless parameters in this case are:

$$Velocity: \phi = \frac{v_x}{v_0}; \qquad Position: \eta = \frac{y}{L}; \qquad Time: \tau = \frac{\nu t}{L^2}$$

where v_0 is the final velocity of the plate [m/s], L is the distance between the two plates [m], ν is the kinematic viscosity [m^2/s], and t is the time in [s].

The derivation of the solution can be found in Bird, Stewart and Lightfoot[12], and the solution is reported here:

$$\phi(\eta,\tau) = (1-\eta) - \sum_{n=1}^{\infty}\left(\frac{2}{n\pi}\right) exp(-n^2\pi^2\tau)\ sin\ (n\pi\eta) \qquad \textit{Equation 3}$$

The first term is the steady-state term and the summation is the transient piece of the solution. The transient term converges quickly—the calculation only needs to be carried out until the ratio of the (n^{th} + 1) term to the summation of n terms is sufficiently small, for example, < 1E-03. A good rule of thumb is to use n = 30.

A simulation was run in Fluent with the transient solver for a moving wall at v_0 = 0.113 m/s. Note: this is not pressure-driven flow, so the periodic pressure gradient was set to 0. Several time points were chosen for analysis. The computational solution was compared to the analytical solution, calculated with the same parameters using Equation 3. The analytical solution was generated through a macro written in Excel Visual Basic, with n = 30 and terms checked for convergence. The comparison of these two solutions at several different time points is shown below.

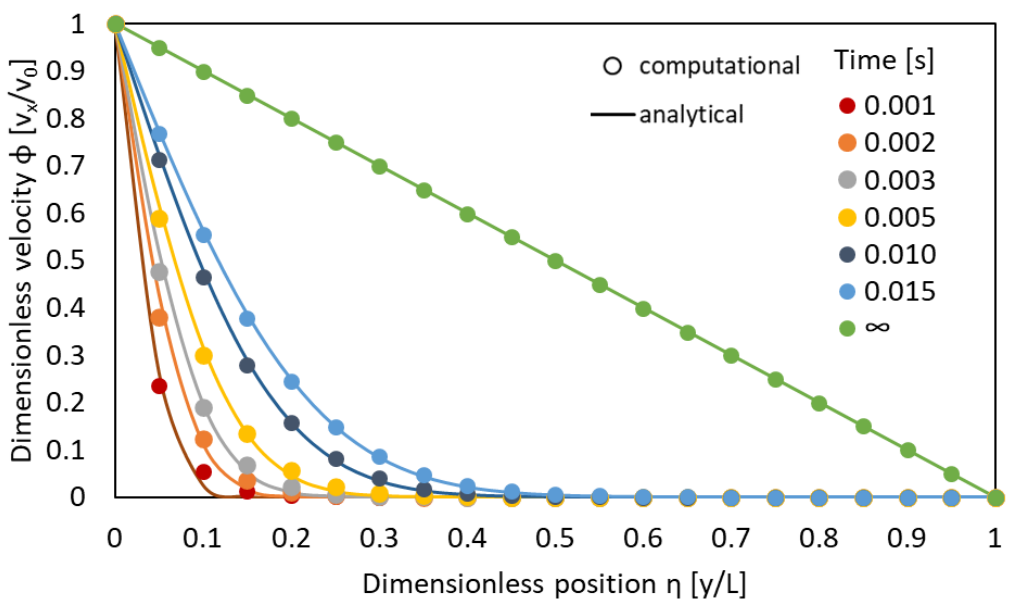

Figure 13: Startup flow between parallel plates. Comparison of computational (points) and analytical (lines) velocity profiles as a function of dimensionless position with time as a parameter. Steady-state (t = ∞) was reached at a simulation time of t = 3 s.

Again, the analytical and computational solutions demonstrate good agreement, with accuracy increasing with increasing time.

3.1.3.2. Cone and Plate

3.1.3.2.1. Steady state

The cone and plate geometry is significantly more complicated than the parallel plate geometry, because of the addition of an independent variable: The velocity profile is now a function of position in the Y (vertical) and XZ (radial) directions, as well as time in non-steady-state cases. However, with the proper simplifications and assumptions, an analytical solution for the wall shear stress can be found.

Sucosky et al pose[48] an analytical expression for the wall shear stress on the surface of the plate in a cone and plate device (CPD). This expression is valid for low Reynolds numbers and small angle α between the cone and the plate. With the presence of a gap h between the cone apex and the plate, the wall shear stress on the plate is spatially dependent, and can be modeled by:

$$\tau_w = \mu\omega\left(\frac{z}{h+z\alpha}\right) \qquad \textit{Equation 4}$$

where τ_w is the shear stress on the surface of the plate [dyne/cm^2], μ is the viscosity of the fluid, ω is the angular velocity in [rad/s], z is the radial position, h is the gap height, and α is the cone angle.

A Fluent run was done for ω = 30 rad/s, h = 0.01 cm, α = 2.5°. The simulation was run with the transient solver for two seconds (~10 rotations) to achieve steady state. The results from the simulation compared to the analytical solution calculated by Equation 4 are shown below for the shear stress profile as a function of radial position Z along the plate.

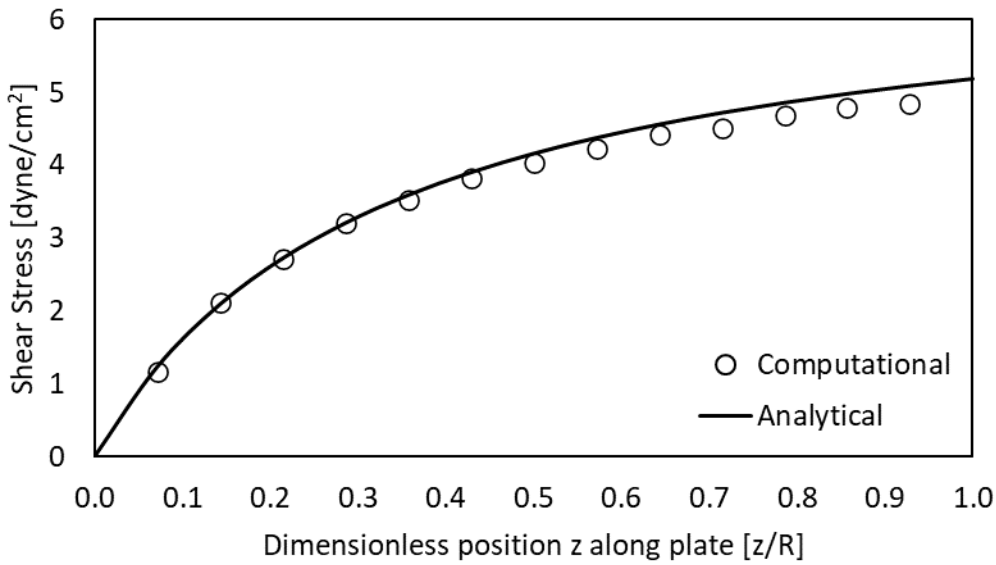

Figure 14: Steady-state rotation of a CPD as a function of radial position. Computational solution (points) compared to the analytical solution (line), calculated from Equation 4. ω = 30 rad/s, h = 0.01 cm, α = 2.5°. Solution given as a function of dimensionless position z/R, where R is the cone radius (R = 0.7 cm).

The difference between the computational and analytical cases are within 5%, except very near the plate edges. This is to be expected, because at the cone apex (z = 0) and cone outer wall (z = 0.7 cm) the presence of end effects generates a secondary flow, compromising the accuracy of the analytical solution.

3.2. Cone and Plate Experiments

3.2.1. CPD setup and validation

3.2.1.1. Description of CPD setup

As previously mentioned, Kouzbari *et al.* built a cone and plate device to test the dependency of latent TGF-β activation on shear stress. The following figure shows the device's design and dimensions:

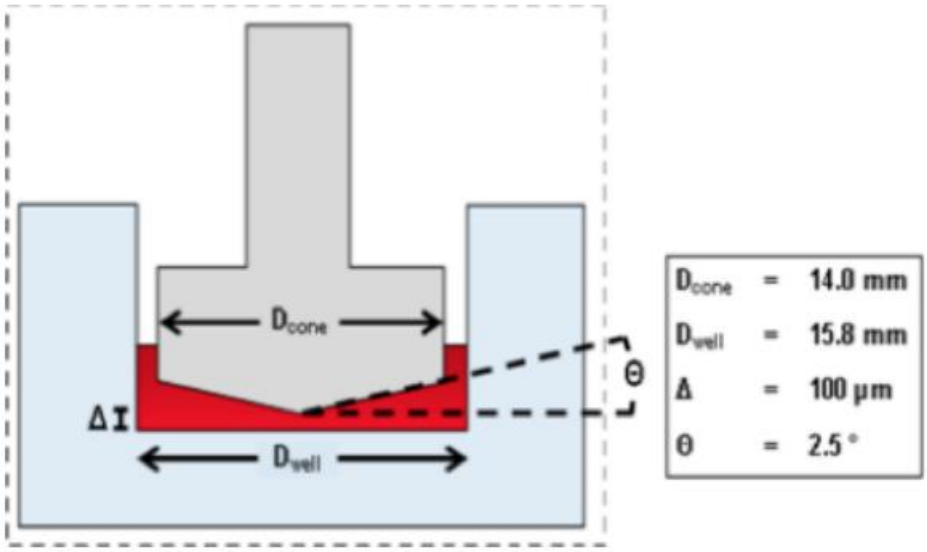

Figure 15: Cone and plate device used in Kouzbari et al. Dimensions shown on the figure include the diameter of the cone and well, the angle between the cone and the plate, and the gap height between the plate and the cone apex. Image from [50].

The cone and plate functionality is as follows[50]:

> We designed and built a cone-and-plate shear device capable of generating either steady shear (SS) or oscillatory shear (OSS) by rotation direction controlled by an Arduino MEGA System connected to a Big Easy Driver stepper motor controller with an ON/OFF rocker switch. The cone is made of Delrin acetal resin to render it biocompatible, and has a 2.5 degree angle and a diameter of 14 mm. The diameter of the plate is 15.8mm, with a gap 0.9mm between the cone and the plate on each side. The cone was connected to a stepper motor (bipolar, 200 steps/rev, NEMA 17 size) via an aluminum shaft coupling. The mounting base for the stepper motor was designed using Solidworks 2017 and 3D printed with poly-lactic acid (PLA) on a Makerbot Replicator 5th generation. An A4988 Allegro-based micro stepping driver (Big Easy Driver) was supplied with 24V DC and connected to an Arduino MEGA 2560-R3 microcontroller to control the stepper motor. The Arduino Integrated Development Environment (IDE; version 1.8.2) was used to program the

microcontroller to switch the rotation mode between SS and OSS, by controlling the rotational velocity, and the period of oscillation/switch rotational direction. (Quoted from [50]).

I reprogrammed this device to test the effect of shear stress generated by different oscillation patterns on the activation of latent TGF-β. The four previously programmed cases were overwritten, and three different types of oscillatory velocity profiles were generated to drive the motor. A fourth case with constant rotation of the cone was programmed for a control. The description of these cases and the validation of the motor that drives the rotation of the cone is presented below. With this reprogramming, this device can now be used in future experiments at the Oklahoma Medical Research Foundation to build on previous results and better understand the mechanisms and triggers that drive TGF-β activation.

3.2.1.2. Motor Validation

The cone and plate device (CPD) was programmed to generate oscillatory shear three different ways. In the first case, the cone rotates in one direction for 0.4 s and then abruptly changes direction with a 0.1 s pause in between, for a total cycle length of 1 s. In the second case, the cone rotates in one direction for 0.4 s and then linearly decelerates for 0.1 s until it is rotating at the same speed in the opposite direction, again for a total cycle length of 1 s. In the third case, the cone rotation is sinusoidal—the boundary condition is given by the following function:

$$\Omega_{cone}(t) = 300\ sin\ (2\pi t) \qquad \textit{Equation 5}$$

This results in a maximum speed of the cone of 300 RPM, a speed safely in the operating range of the motor, and a period of 1 s. A fourth case, of unidirectional steady rotation, was used as a control. The velocity profiles of these cases are shown in the figure below.

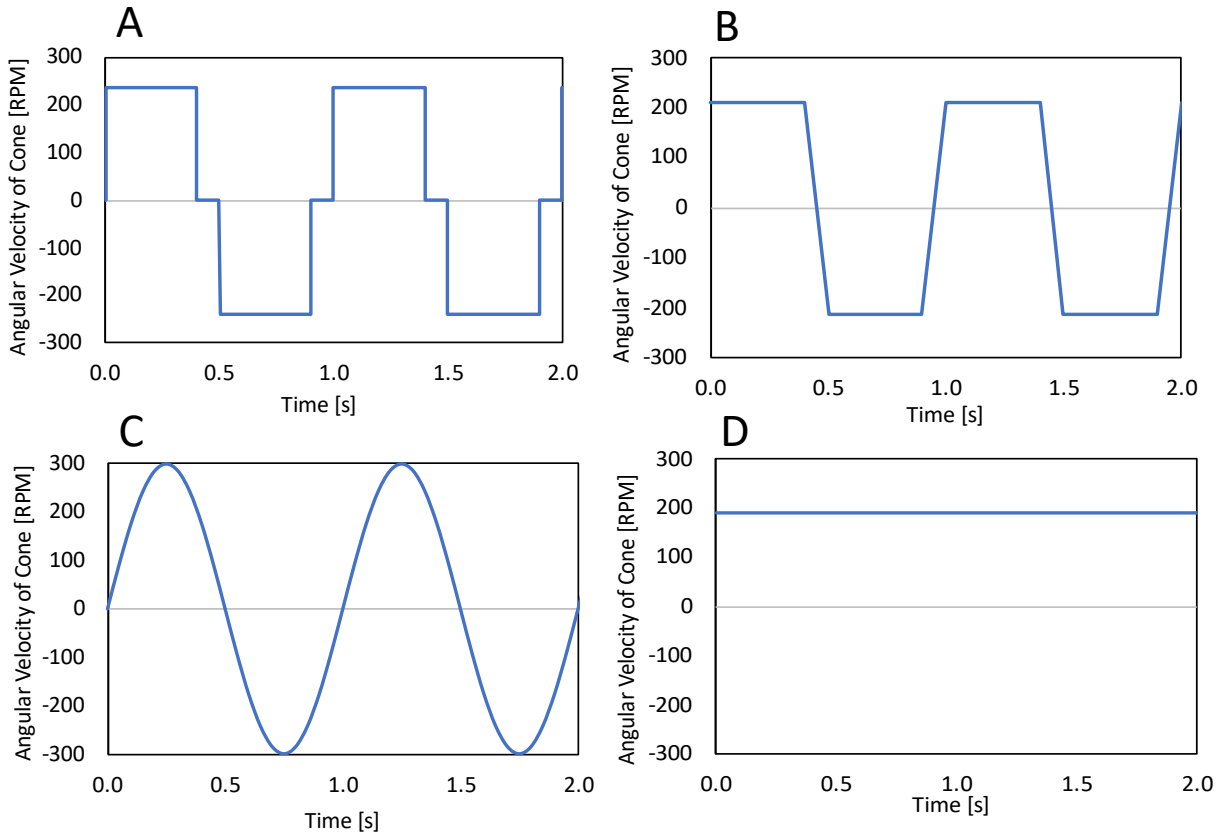

Figure 16: Velocity profiles for the different cases programmed on the CPD. 2 periods of rotation shown. A) Oscillation with an abrupt change in direction. B) Oscillation with ramped acceleration/deceleration. C) Sinusoidal oscillation. D) Constant unidirectional rotation (steady shear; control case). Positive RPMs indicate counterclockwise (CCW) rotation; negative RPMs indicate clockwise (CW) rotation of the cone.

The maximum speed (in RPMs) for the four cases were determined by first setting the sinusoidally oscillating case to Ω_{cone} = 300 RPM, a speed close to the maximum speed at which the motor can consistently operate. From there, the other cases' speeds were set by matching the integrals of the profiles to that of the sinusoidal case (see 3.2.2 for more details). This resulted in a maximum angular velocity of 240 RPM for the abrupt case, 212 RPM for the ramped case, and 190 RPM for the constant case.

The Arduino code used to drive the motor for each of these cases can be found in the Appendix. Once the CPD was programmed correctly, an external encoder (Rotary Encoder- 1024

P/R Quadrature) was used to validate the device's operation. A model showing the CPD-encoder assembly for testing is shown below.

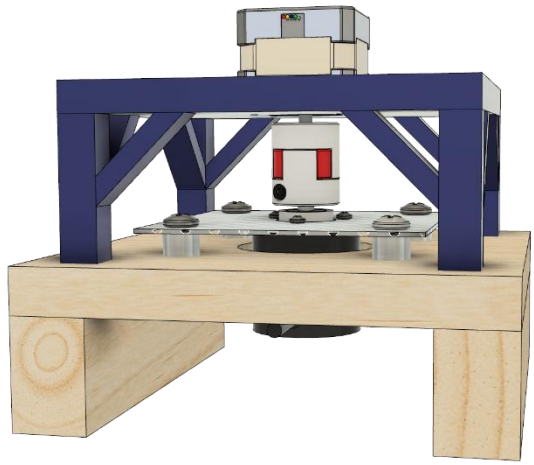

Figure 17: Fusion 360 model showing the CPD used in experiments mounted to an external encoder for validation tests.

The encoder was driven by the motor shaft and an Arduino Uno was used to read the position of the encoder, outputting a time (in μs) and increment of "ticks" every time the motor took a step. There are 1024 ticks per 1 rotation of the motor. These data were then read into MatLab and converted to RPM(t) by the following equation:

$$RPM(t_n) = \frac{ticks_{t_{n+1}} - ticks_{t_{n-1}}}{t_{n+1} - t_{n-1}} * \frac{1\ rotation}{1024\ ticks} * \frac{1E06\ \mu s}{1\ s} * \frac{60\ s}{1\ min} \qquad \textit{Equation 6}$$

The encoder-generated RPM profiles of the motor were plotted against the velocity profiles shown above. The results for the four cases are shown below:

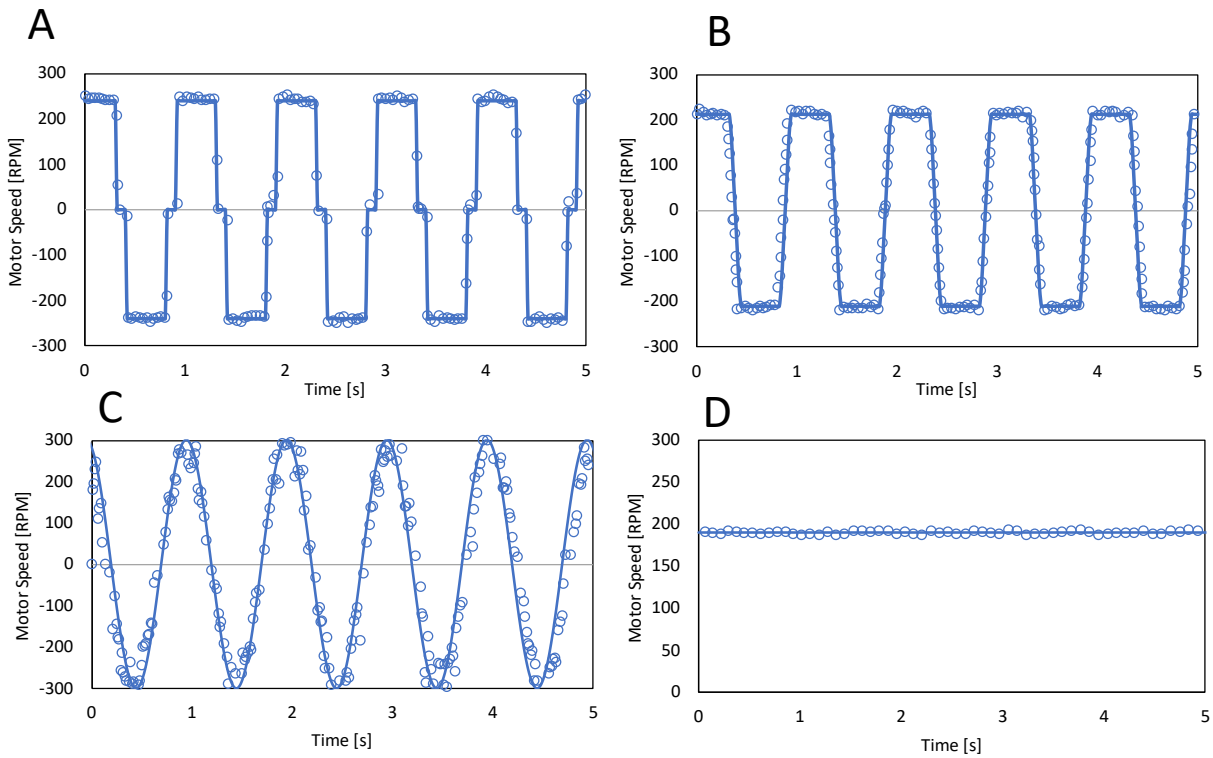

Figure 18: CPD validation. Circles indicate encoder data; lines indicate modeled profile. A) Oscillation with an abrupt change in direction. B) Oscillation with ramped acceleration/deceleration. C) Sinusoidal oscillation. D) Constant unidirectional rotation (steady shear; control case). Positive RPMs indicate counterclockwise (CCW) rotation; negative RPMs indicate clockwise (CW) rotation of the cone.

As can be seen from the graphs, the encoder data are in excellent agreement with the desired profiles. This means we can say with confidence that the motor is producing the target oscillatory profiles with high accuracy.

While each case will only be operated at one motor speed, it is also worth checking that the cases work consistently across the whole range of RPMs. Therefore, tests were run at 100, 200, and 300 RPM for each of the four cases. The results for the ramped case are shown below.

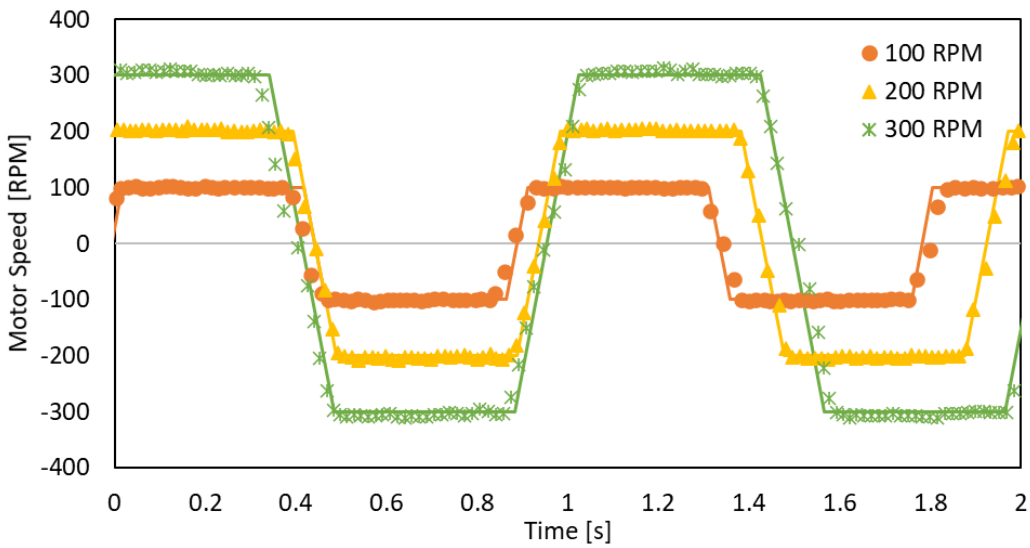

Figure 19: Validation across the range of RPMs for the ramped case. Experimental data (points) and target profiles (lines) for the ramped case with a maximum motor speed of 100, 200, and 300 RPM. In all cases, acceleration is the same (4240 RPM/s).

Additional tests were run to check for operational consistency of the motor over time. The abrupt case was run for two hours, with data taken every 30 minutes to check that the motor's operation does not drift over time. The results from this test are shown below.

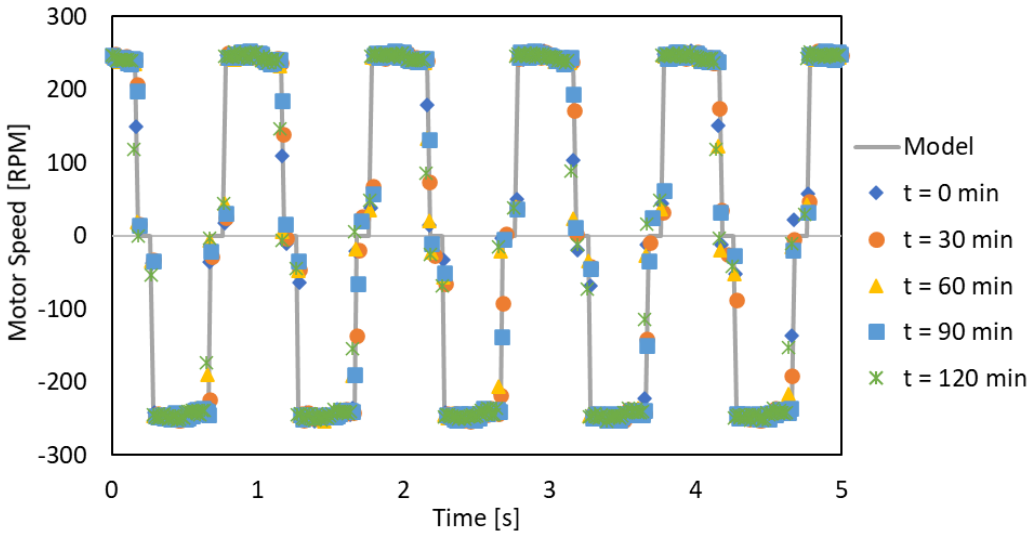

Figure 20: Motor validation over time for the abrupt case. 5 s of data taken every 30 minutes for 2 hours. Data (points) compared to the modeled profile (line).

As the figure shows, the motor runs remain consistent even over longer periods of time. Most importantly, the motor reaches the same maximum speed (240 RPM) every cycle—it does not deviate from its programmed value.

In sum, the motor's performance in the CPD has been validated to work for three different cases of oscillatory motion, as well as a constant control case. It works at the specific RPMs for each case, across the entire range of RPMs, and over long periods of time.

3.2.2. Shear Stress Calculations

Fluent was used to generate velocity profiles as a function of position and time. Those velocity profiles were then used to manually calculate the shear stress in the fluid. Fluent calculates Wall Shear Stress, but calculating the shear stress throughout the whole fluid must be done manually. The shear stress was calculated using Equation 1 (Newton's law of viscosity). The shear rate (dv/dy) was calculated using one of the following finite difference formulas, based on whether the data point of interest was the first, last, or in the middle of the dataset.

$$\textit{Forward: } f'(x) = \frac{-3f(x)+4f(x+\Delta x)-f(x+2\Delta x)}{2\Delta x} \qquad \textit{Equation 7}$$

$$\textit{Backward: } f'(x) = \frac{3f(x)-4f(x-\Delta x)+f(x-2\Delta x)}{2\Delta x} \qquad \textit{Equation 8}$$

$$\textit{Centered: } f'(x) = \frac{f(x+\Delta x)-f(x-\Delta x)}{2\Delta x} \qquad \textit{Equation 9}$$

Several types of oscillatory cases are tested in this report—abrupt stop, ramped acceleration, and sinusoidal. To maintain continuity between these cases, the maximum value of the velocity in each case was chosen such that the integral of the velocity profile remains the same. Note that this choice is somewhat arbitrary because we do not know the specific differences in shear are generate different responses in latent TGF-β activation. By keeping the integral of the

velocity profile constant, we can obtain shear stress profiles with very similar averages but different peaks.

The cases for each geometry were normalized to the sinusoidal case. This case has a continuous (as opposed to step-wise) velocity profile, so the integral could be calculated analytically. The general form of the sinusoidal boundary condition for the velocity is as follows:

$$v(t) = A * sin(2\pi t) \qquad \textit{Equation 10}$$

where A is the maximum velocity in units of either linear velocity [m/s], or angular [rad/s]. In the parallel plate geometry A is set to 1 m/s and in the cone and plate geometry it is set to 31.4 rad/s (300 RPM). This function has the following integral:

$$\int_0^{0.5} A * sin(2\pi t)\, dt = \frac{A\, sin^2(0.5\pi)}{\pi} \qquad \textit{Equation 11}$$

This integral is evaluated for the first half of the sine curve (t = 0 to t = 0.5), because it is the positive area (the integral of the entire sine curve would just be zero).

The value of A = 1 m/s was chosen for the parallel plate geometry based on the peak velocity of forward flow in the aortic valve. Peak velocity of forward flow is about 1.0 m/s in a normal aortic valve[56], so this was chosen as the maximum velocity of the plate. The value of A = 300 RPM is chosen for the cone and plate geometry because it is the maximum speed that the motor driving the physical cone and plate device should operate at.

Under normal physiological flow conditions, the wall shear rate in blood vessels ranges from ~10 – 2000 s^{-1}.[57] The shear rates used in this thesis are on the order of 500-700 s^{-1} in the cone and plate device and 600-1000 s^{-1} in the parallel plate geometry, which are well within this range. Reports of peak wall shear stress on aortic valve leaflets vary from 20 to over 1000 dyne/cm^2.[58] This large range has to do with where measurements are taken, the nature of the flow in which the valve was functioning, and whether it was natural or prosthetic. It is probable that this range is

closer to 100-200 dyne/cm^2.[58] The simulations in this report have peak shear stresses between 20-200 dyne/cm^2.

4. Computational Results

4.1. Parallel Plates

4.1.1. Abruptly oscillating plate

The parallel plate was set to oscillate with abrupt changes in direction. It moves for 0.4 seconds in the +X direction, pauses for 0.1 seconds, and moves in the -X direction for 0.4 seconds, followed by another 0.1 second pause, for a total cycle length of 1 second. The plate's velocity is set to ± 0.79577 m/s. This value was chosen because it produces an integral of the velocity profile equal to that of a sinusoidal velocity profile with a maximum velocity of 1 m/s. These values are summarized in the table below:

Table 5: Summary of case variables for the abrupt oscillation of a parallel plate

Variable	Value
Case Type	Abrupt
Plate maximum velocity	0.79577 m/s
Hold time	0.4 s
Stop time	0.1 s

The velocity of the fluid in the direction of motion (V_x) produces shear stresses on the fluid particles. The shear stress is calculated using the following reduction of Newton's law of viscosity:

$$\tau = \mu * \frac{dv_x}{dy} \qquad \textit{Equation 12}$$

where τ is the shear stress in [dyne/cm^2], μ is the viscosity of the fluid (1.0019E-02 cP), and dv_x/dy is the shear rate in [s^{-1}]. The velocity and shear stress profiles are shown below. Note: The simulation results are from the third period; two periods of oscillation were run first to ensure the damping of any start-up effects, allowing the simulation to reach pseudo-steady state. This will be the case for all results shown.

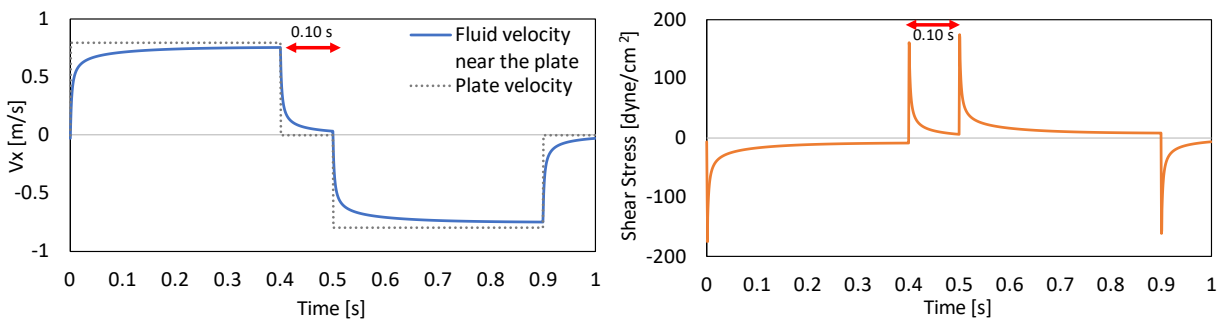

Figure 21: Velocity and shear stress profiles generated by an abruptly oscillating parallel plate. Left: Velocity of the plate (dotted line) and velocity of the fluid just below the moving plate (solid line; y/y_{plate} = 0.95). Right: Shear stress of the fluid at the wall. The 0.10 s stop time is labeled on both graphs with a red arrow.

As can be seen from the figure, the stopping of the plate generates a spike in shear stress, as does the resumption of motion. This spike can be seen in the opposite direction when the plate motion is stopped/resumed from motion in the opposite direction, but with the same magnitude. The shear stress reaches a peak value of 175 dyne/cm^2, although it averages just 16.9 dyne/cm^2 over the entire 1 second period.

The above graphs show the velocity and shear stresses at the plate as a function of time. An alternative way to conceptualize the data is to look at the velocity and shear stress profiles over the entire gap between the two plates at different time points (Figure 22, below).

The velocity profiles at the time points in the middle of the 0.4 second holding periods (0.25 and 0.75 seconds) approach linearity. This result approaches the analytical solution to the case of parallel plates with one plate moving unidirectionally at a constant speed. The

corresponding shear stresses are relatively low and constant in the entire distance between the plates, decreasing slightly closer to the stationary plate.

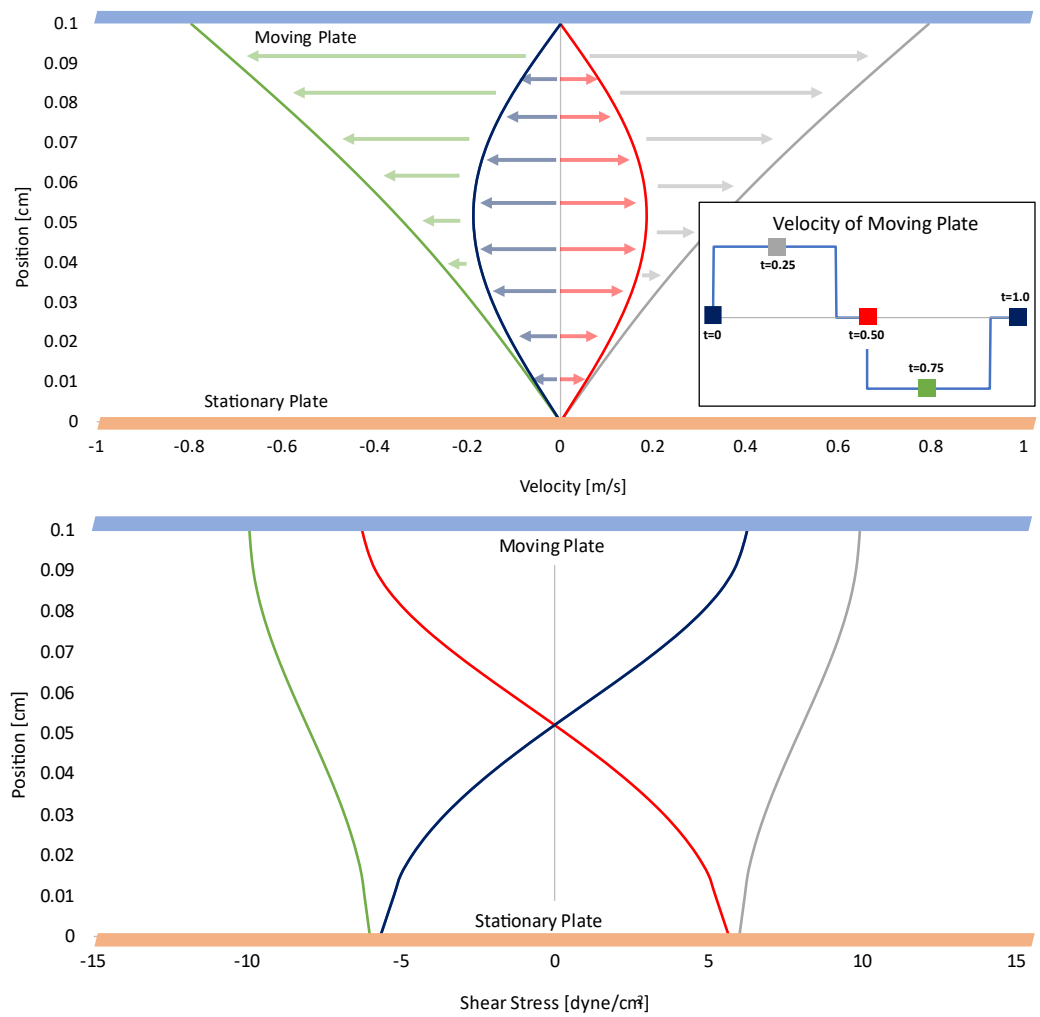

Figure 22: Velocity and shear stress of the fluid between two parallel plates at different time points. Top: Velocity profile. Colored arrows show the direction that the fluid is moving for each given time point. Bottom: Shear stress profile. Inset: Velocity profile of the abruptly oscillating plate. Colored points correspond to the colored curves on the graphs. Time points taken at t = 0, 0.25, 0.50, 0.75, and 1.0 s. The maximum velocity of the plate is ±0.80 m/s. The moving plate is depicted as a blue rectangle, and the stationary plate as an orange rectangle.

The velocity profiles at the transition points (t = 0, 0.50, 1.0 s), where the plate's motion is suspended (v_{plate} = 0 m/s), are parabolic. Because this motion is periodic, the velocity profiles at t = 0 and t = 1 second are identical. The curve is inverted at t = 0.50 seconds because the fluid had just been flowing in the opposite direction as at t = 0 and 1. Parabolic flow is expected here because

when both plates are stationary, the fluid will be moving fastest at the point farthest away from the plates. The shear stress profiles calculated at these times show an inflection point in the center of the gap between the plates, which is where the velocity is a maximum.

What the above graphs are missing, however, is how the shear stress and velocity profiles appear when the shear stress reaches its maximum magnitude. In the cycle, this occurs twice—both times in the instant the plate's motion has been restarted.

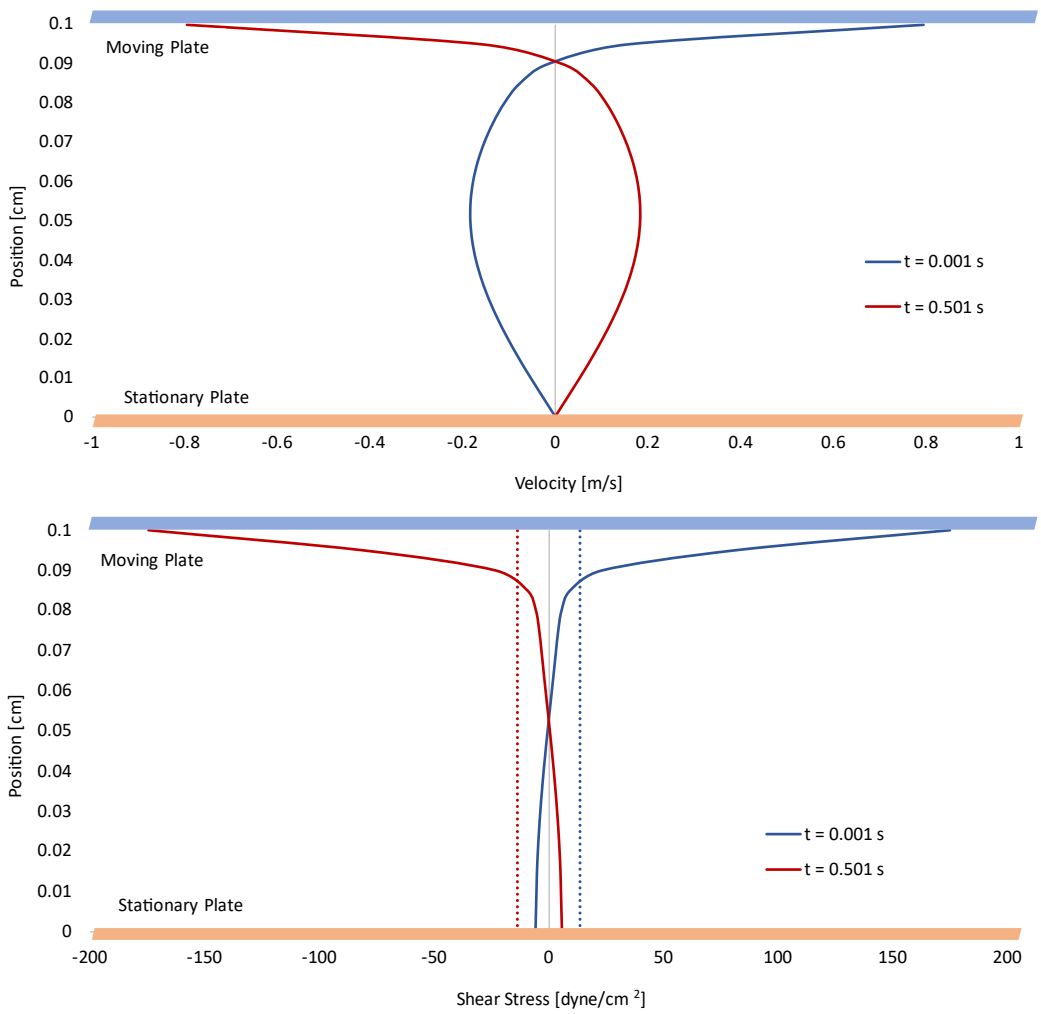

Figure 23: Velocity and shear stress profiles for an abruptly oscillating plate just after plate motion has been restarted (t = 0.001, 0.501 s). Top: Velocity of the fluid between the plates. Bottom: Shear stress of the fluid between the plates. Dashed lines: the position-averaged shear stress for each time. The moving plate is depicted as the blue rectangle, and the stationary plate as an orange rectangle.

As can be seen from Figure 23, the abrupt spike in shear stress caused by the abrupt change in plate motion does not propagate very far into the fluid—in fact, only 10% of the fluid domain experiences shear stress magnitudes above the average. This spike in shear stress, however, is significant—note the difference in scale in the X-axis of Figure 22 vs Figure 23: there is a 13-fold increase.

Overall, abrupt oscillatory motion of a parallel plate generates spikes of high shear stress, although this elevated shear stress does not last for very long or propagate very far into the fluid.

4.1.2. Ramped acceleration/deceleration of oscillating plate

The parallel plate was set to oscillate with linear acceleration/deceleration during changes in direction. It moves with a velocity $+v_{plate}$ for 0.4 seconds in the +X direction, decelerates to $-v_{plate}$ for 0.1 seconds, stays at $-v_{plate}$ in the -X direction for 0.4 seconds, and accelerates back to $+v_{plate}$ in another 0.1 seconds, for a total cycle length of 1 second. The plate's velocity is set to $v_{plate} = \pm 0.70736$ m/s. This value was chosen because it produces an integral of the velocity profile equal to that of a sinusoidal velocity profile with a maximum velocity of 1 m/s. These values are summarized in the table below:

Table 6: Summary of case variables for the ramped oscillation of a parallel plate

Variable	Value
Case Type	Ramped
Plate maximum velocity	0.70736 m/s
Hold time	0.4 s
Ramp time	0.1 s

The velocity profile, as well as the shear stress profile (calculated as in Equation 12) for this case are shown in Figure 24.

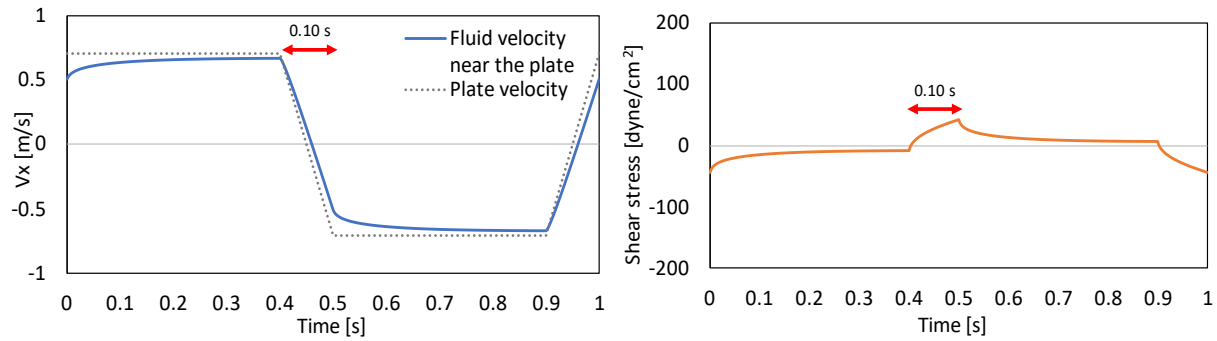

Figure 24: Velocity and shear stress profiles generated by an oscillating parallel plate with ramped acceleration. Left: Velocity of the plate (dotted line) and velocity of the fluid at y/y_{plate} = 0.95 (solid line). Right: Shear stress of the fluid at the wall. The 0.10 s stop time is labeled on both graphs with a red arrow.

As can be seen from the figure, changing the velocity of the plate causes a temporary increase in shear stress. The shear stress reaches a peak value of 43.2 dyne/cm^2, averaging 15.1 dyne/cm^2 over the entire 1 second period.

The above graphs show the velocity and shear stresses at the plate as a function of time. An alternative way to conceptualize the data is to look at the velocity and shear stress profiles over the entire gap between the two plates, at different times (Figure 25).

In Figure 25, the velocity profiles at the time points in the middle of the 0.4 second holding periods (0.25 and 0.75 seconds) approach linearity, very similarly to how they did in the abrupt case. This approaches the analytical solution of the velocity profile of flow between parallel plates with one plate moving at a constant speed in one direction. The corresponding shear stresses are relatively low and constant in the entire distance between the plates, decreasing slightly closer to the stationary plate.

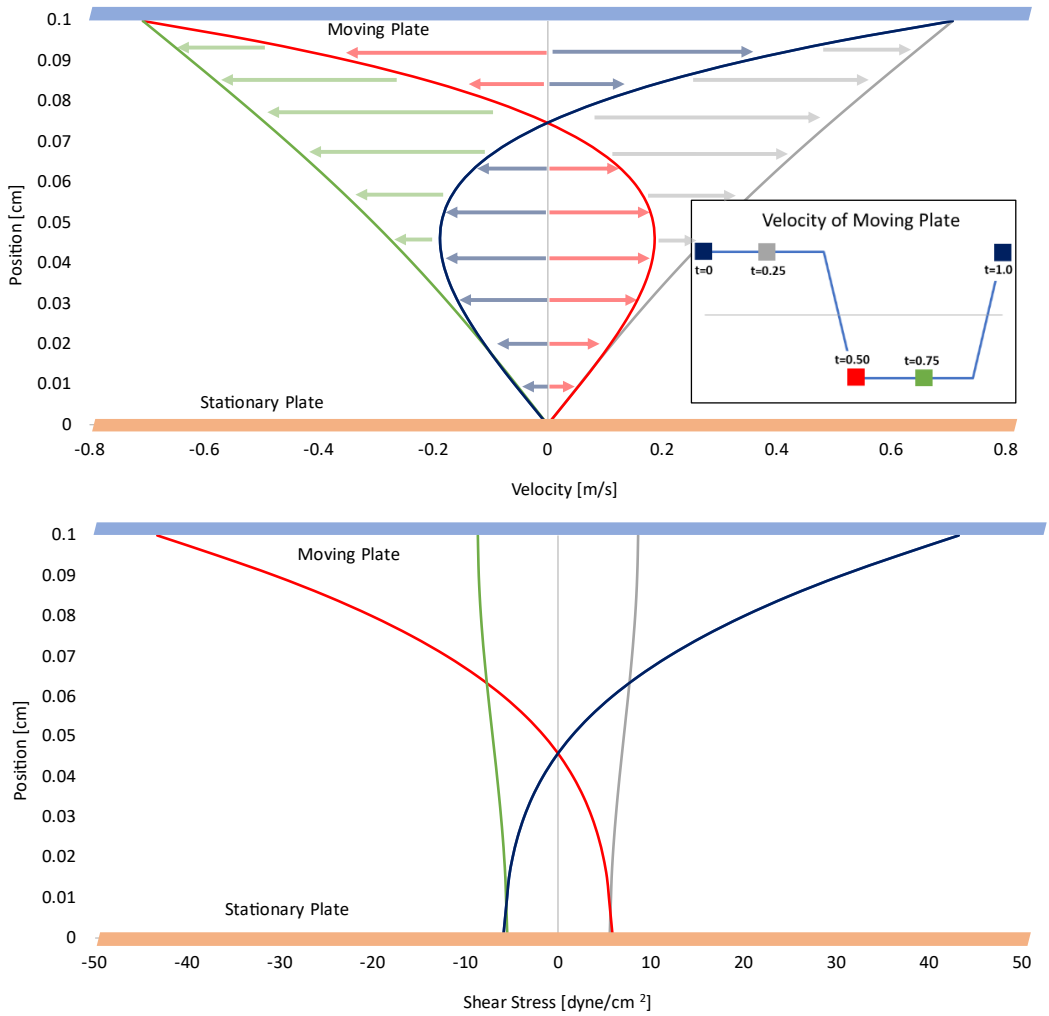

Figure 25: Velocity and shear stress of the fluid between two parallel plates with oscillatory motion and ramped acceleration at different time points. Top: Velocity profile. Colored arrows show the direction that the fluid is moving for each given time point. Bottom: Shear stress profile. Inset: Velocity profile of the plate for the ramped case. Colored points correspond to the colored curves on the graphs. Time points taken at t = 0, 0.25, 0.50, 0.75, and 1.0 s. The maximum velocity of the plate is ±0.71 m/s. The moving plate is depicted as a blue rectangle, and the stationary plate as an orange rectangle.

The velocity profiles taken at points immediately after a ramped acceleration/deceleration period (t = 0.0, 0.5, 1.0 s), when the plate has reached its maximum speed, are bidirectional. At those instances (the blue and red curves on the figures above), most of the fluid shows the typical (if slightly skewed) parabolic velocity profile. In the top quarter of the gap between the plates, however, the fluid velocity is actually already moving in the other direction, reflecting the fact that

the plate has recently changed direction. This extreme shift is reflected in the shear stress profiles, which reaches a maximum (43.2 dyne/cm^2) on the wall at these times.

Overall, oscillatory motion of a parallel plate with ramped acceleration/deceleration generates a spike in shear stress much lower than the abrupt case, with the maximum shear stress occurring immediately after the acceleration periods.

4.1.3. Sinusoidally oscillating plate

The plate was then programmed to oscillate smoothly, using a sinusoidal function. After adjusting a sine curve to have a period of 1 second and an amplitude of 1 m/s, the following equation for the velocity of the plate was developed:

$$v_{plate}(t) = 1\frac{m}{s} * sin\,(2 * \pi * t) \qquad \textit{Equation 13}$$

where t is in [s], and v_{plate} is in [m/s]. This velocity profile, as well as the corresponding shear stress profile, is shown below.

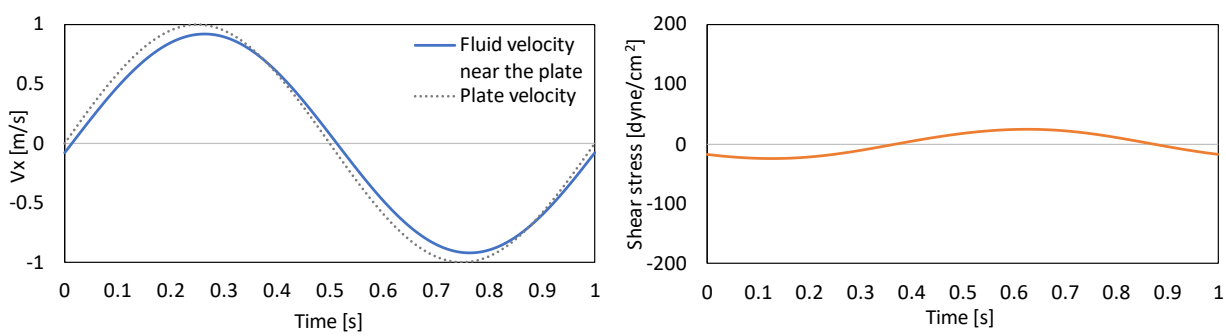

Figure 26: Velocity and shear stress profiles generated by a sinusoidally oscillating parallel plate. Left: Velocity of the plate (dotted line) and velocity of the fluid at y/y_{plate} = 0.95 (solid line). Right: Shear stress of the fluid at the wall.

The shear stress profile is roughly an inverted sine curve, with a maximum value of 23.9 dyne/cm^2 and a magnitude averaging 15.3 dyne/cm^2 across the 1 second period. The velocity and shear stress profiles as functions of position at the critical points of the velocity profile (maximum, minimum, and zeroes) are shown in Figure 27 below.

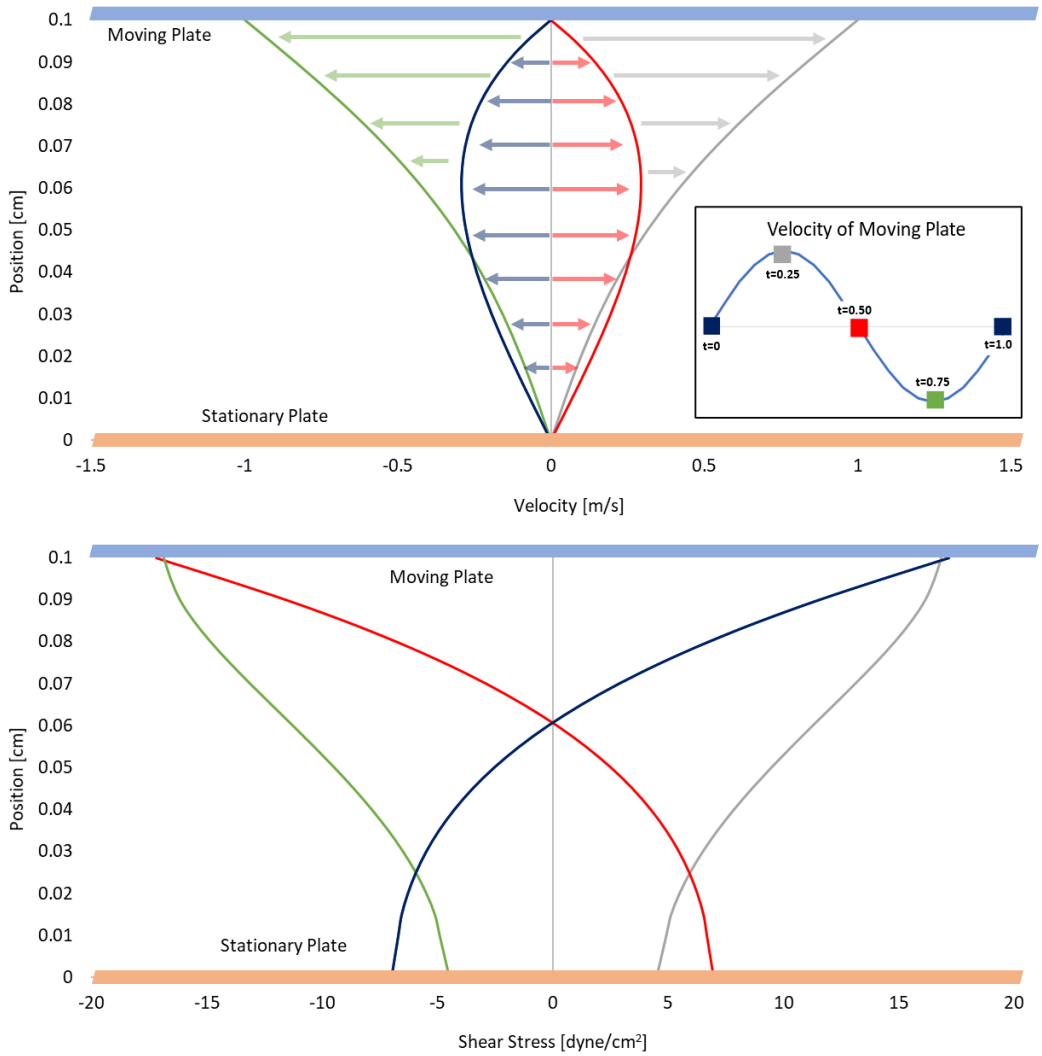

Figure 27: Velocity and shear stress of the fluid between two parallel plates with sinusoidal oscillatory motion at different time points. Top: Velocity profile. Colored arrows show the direction that the fluid is moving for each given time point. Bottom: Shear stress profile. Inset: Velocity profile of the plate for the sine case. Colored points correspond to the colored curves on both graphs. Time points taken at t = 0, 0.25, 0.50, 0.75, and 1.0 s. The maximum velocity of the plate is ±1.0 m/s. The moving plate is depicted as a blue rectangle, and the stationary plate as an orange rectangle.

The velocity profile in Figure 27 is very similar to that of the abrupt stopping case, with roughly parabolic profiles at the points where the plate is stopped and profiles approaching linearity at the maximum and minimum velocities.

The shear stresses at the transitions between rotational directions (i.e., counterclockwise to clockwise) that occur at t = 0, 0.5, and 1.0 seconds, are bidirectional. This means that any proteins

in the fluid when testing in a real CPD would experience opposing shear stress every 0.5 seconds, causing a high molecular strain that would accumulate over time and could be a critical factor in higher TGF-β activation[50].

Additionally, in the sinusoidal case the shear stress profile remains a smooth curve, without the spikes characteristic of the abrupt case. It is much more similar quantitatively to the ramped acceleration case, although qualitatively, the two shear stress profiles do look different.

4.1.4. Changing stop time

Next, we investigated the effect of changing the transition time on the shear stress profiles—the stop time in the abruptly oscillating case and the acceleration time in the ramped acceleration case. Three time-lengths were chosen for analysis: 0.01 s, 0.05 s, and 0.10 s. As before, the maximum plate velocity for each case was chosen so that the integrals of the velocity profiles stayed constant. The maximum plate velocities of each case are summarized below.

Table 7: Summary of plate velocities for the abrupt and ramped cases tested at different stopping/acceleration times.

Stop/Acceleration Time [s]	Abrupt Case plate velocity [m/s]	Ramped Case plate velocity [m/s]
0.01	±0.64961	±0.64305
0.05	±0.70736	±0.67013
0.10	±0.79577	±0.70736

The shear stress profiles of the abrupt and ramped cases are compared directly for the three given time periods.

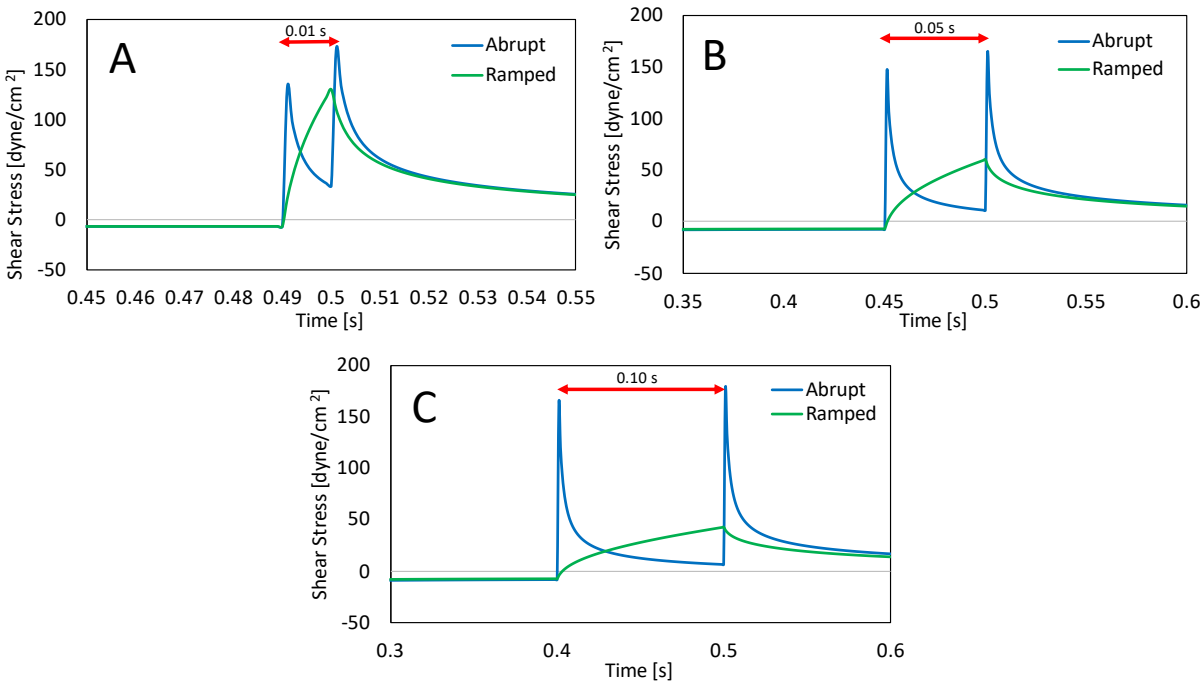

Figure 28: Shear stress profiles of the abrupt oscillation and oscillation with ramped acceleration/deceleration of parallel plates. A) 0.01 second pause/acceleration time. B) 0.05 second pause/acceleration time. C) 0.10 second pause/acceleration time. Abrupt stopping cases shown in blue; ramped acceleration cases shown in green. Stop time labelled with a red arrow.

The effect of stop time in the abrupt case is small—the maximum and average shear stresses do not vary greatly with increasing stop time. In contrast, the ramped acceleration cases have similar averages, but maximum shear stress decreases with increasing start time. Quantitatively, the averages between the abrupt and ramped cases are very similar, but the ramped cases have much lower spikes in shear stress. These statistics are summarized in the following table.

Table 8: Maximum and average shear stresses for the abrupt and ramped cases with different stop/acceleration times.

	Abrupt Stop		Ramped Acceleration	
Stop/Acceleration Time [s]	Maximum shear stress [dyne/cm^2]	Average shear stress [dyne/cm^2]	Maximum shear stress [dyne/cm^2]	Average shear stress [dyne/cm^2]
0.01	169	15.0	130	15.0
0.05	161	15.8	60.2	15.0
0.10	175	16.9	43.2	15.1

The maximum shear stress in the abrupt case increases slightly with increasing stop time, while in the ramped case the maximum shear is much lower at longer acceleration times. Across all cases, the average shear stress remains nearly constant, which makes sense because of the way the maximum velocities were calculated. Thus, a comparison between the abrupt and ramped cases at a given stop time provide a way to observe whether TGF-β activation depends on high spikes in shear stress or is just based on an average.

4.1.5. Reynolds number analysis

The Reynolds number (Re) is a dimensionless quantity that describes the ratio between inertial and viscous forces in a fluid. It serves as an indicator of the amount of turbulence present in a flowing fluid. For parallel plate geometry, the Reynolds number is calculated as

$$Re = \frac{\rho * v * B}{\mu} \qquad \textit{Equation 14}$$

where ρ and μ are the density (998.2 kg/m^3) and viscosity (0.001003 kg/m/s) of the fluid, v is the maximum velocity of the fluid, and B is the size of the gap between the two plates (1E-03 m).

An analysis of the effect of Re on the shear stress profiles generated by oscillatory motion of the plate was done using the abrupt stopping for 0.10 s case. The Re was dropped several orders of magnitude, by changing either the maximum velocity the plate was set to move, or the viscosity of the fluid. Cases were run for Re = 800 (v_{plate} = 7.96E-01 m/s; μ =0.001003 kg/m/s); Re = 8 (v_{plate} = 7.99E-03 m/s; μ =0.001003 kg/m/s); Re = 0.08 (v_{plate} = 7.96E-05 m/s; μ =0.001003 kg/m/s); and Re = 0.08 (v_{plate} = 7.96E-01 m/s; μ = 10.02 kg/m/s). Results are shown below.

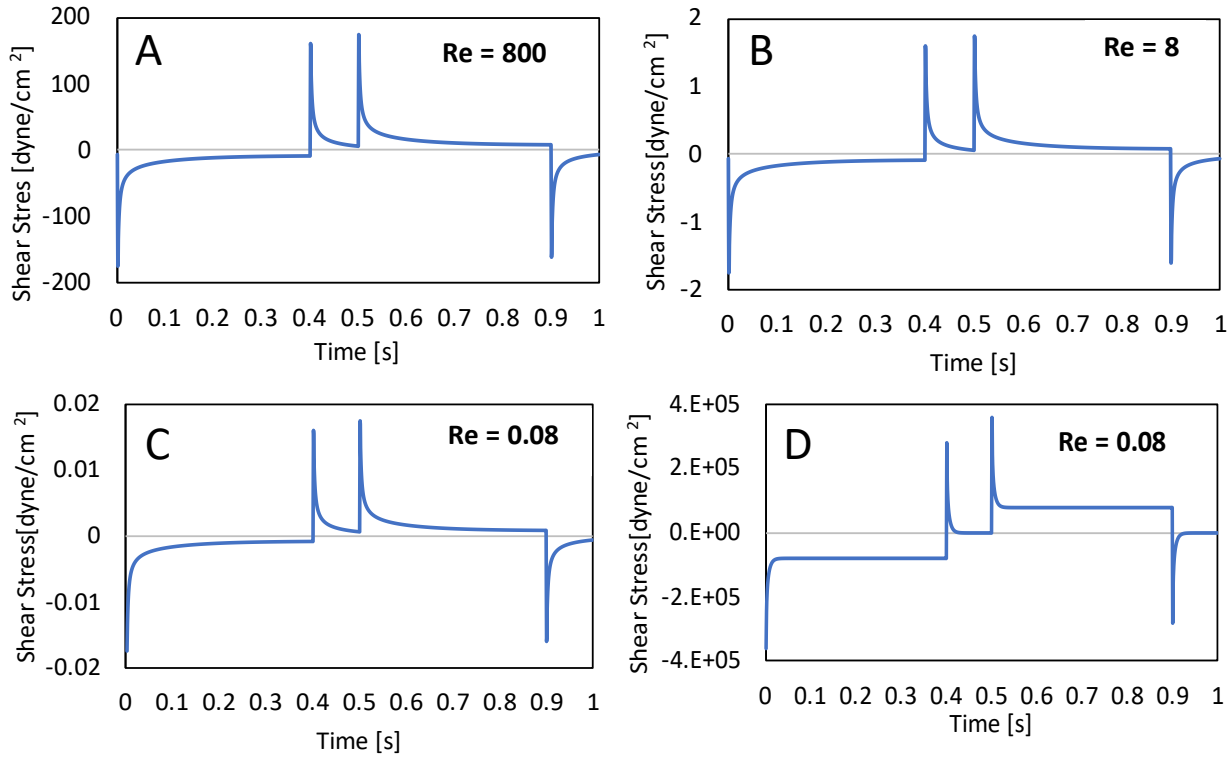

Figure 29: Shear stress profiles at the moving plate for an abruptly oscillating plate at different Re. A) Re = 800; v_{plate} = 7.96E-01 m/s; μ =0.001003 kg/m/s. B) Re = 8; v_{plate} = 7.99E-03 m/s; μ =0.001003 kg/m/s. C) Re = 0.08; v_{plate} = 7.96E-05 m/s; μ =0.001003 kg/m/s. D) Re = 0.08; v_{plate} = 7.96E-01 m/s; μ = 10.02 kg/m/s.

In the first three cases, where Re is changed by changing the velocity of the plate (and therefore the maximum velocity of the fluid), the shear stress profiles have the same behavior and the shear stress magnitudes scale with Re. This finding is somewhat surprising—even as inertial forces are greatly reduced, there is still a clear spike in shear stress even when the fluid velocity is extremely low. To test if this finding was consistent, the fourth case was done, increasing fluid viscosity instead of decreasing velocity and keeping an extremely low Re. The shear stress magnitudes are extremely large (recall that shear stress is a function of viscosity), but the profile shape remains mostly unchanged.

In sum, these profiles remain qualitatively similar even if the velocity changes by orders of magnitude. This has the important implication that even if biological values differ from the 1.0

m/s chosen for models in this report, the trends found here are still applicable. While 1.0 m/s is the typical velocity of the fluid near a normal aortic valve, this value can increase as much as 4x in stenotic valves[56], and other studies have found the maximum speed of valve opening and closure to be on the order of 20 cm/s, which is about an order of magnitude lower[59].

4.2. Cone and Plate

Simulations were run in Fluent in a cone and plate device with geometry matching that of the CPD used in experiments (see 3.2). Cases were run to understand the shear stress profiles generated by oscillatory motion of the cone analogous to those run with the parallel plate geometry in the preceding section, but at lower speeds to match the physical constraints of the motor driving the CPD.

The summary variables for the three cases are shown in the table below. In all cases, the oscillation is cyclical with a period of 1 second. The abrupt and ramped cases have a hold time of 0.4 s at their maximum angular velocity and a stop/acceleration time of 0.1 s.

Table 9: Maximum angular velocities for each oscillatory profile type in the CPD geometry. Values given in rad/s and in RPMs (parentheses).

Case Type	Maximum Angular Velocity ω [rad/s] (RPM)
Abrupt	25.0 (240)
Ramped	22.2 (212)
Sinusoidal	31.4 (300)

This geometry is 3-dimensional, but radially symmetric. Therefore, when running simulations in Fluent, a cross-section was taken at Z = 0, with points chosen for analysis along the X and Y axis.

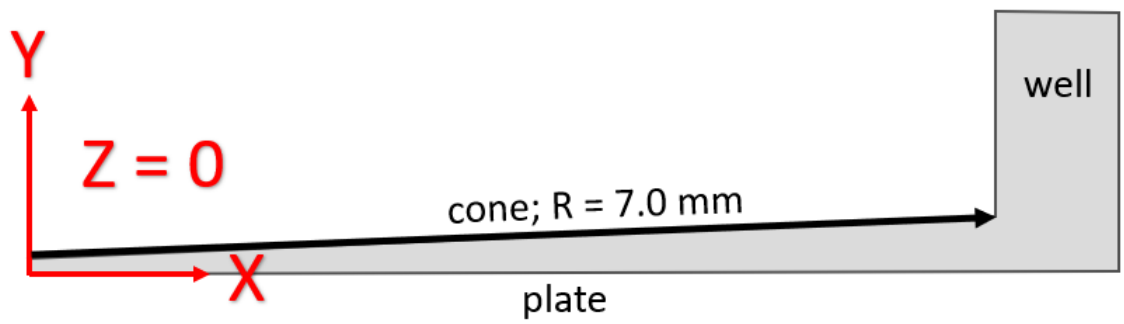

Figure 30: Cross-section of the CPD taken at Z = 0. Coordinate axes and basic components of the CPD geometry labeled. The black arrow along the length of the cone is indicative of where data were taken.

In this geometry, velocity is changing with position in the radial (XZ) and vertical (Y) directions, as well as with time. The velocity profile was generated in Fluent and the shear stress was calculated as

$$\tau(z, y, t) = \mu * \frac{dv_z}{dy}|z \qquad \textit{Equation 15}$$

There is a non-zero X-component of the velocity, but it is negligible compared to the Z-component, because it is, on average, several orders of magnitude smaller.

The shear stress in the fluid will be the highest at the surface of the cone, which is where velocities are highest. Therefore, the shear stress was calculated at the surface of the cone as a function of both radial position on the cone (X) and time. The velocity and corresponding shear stress profiles for each case are shown below.

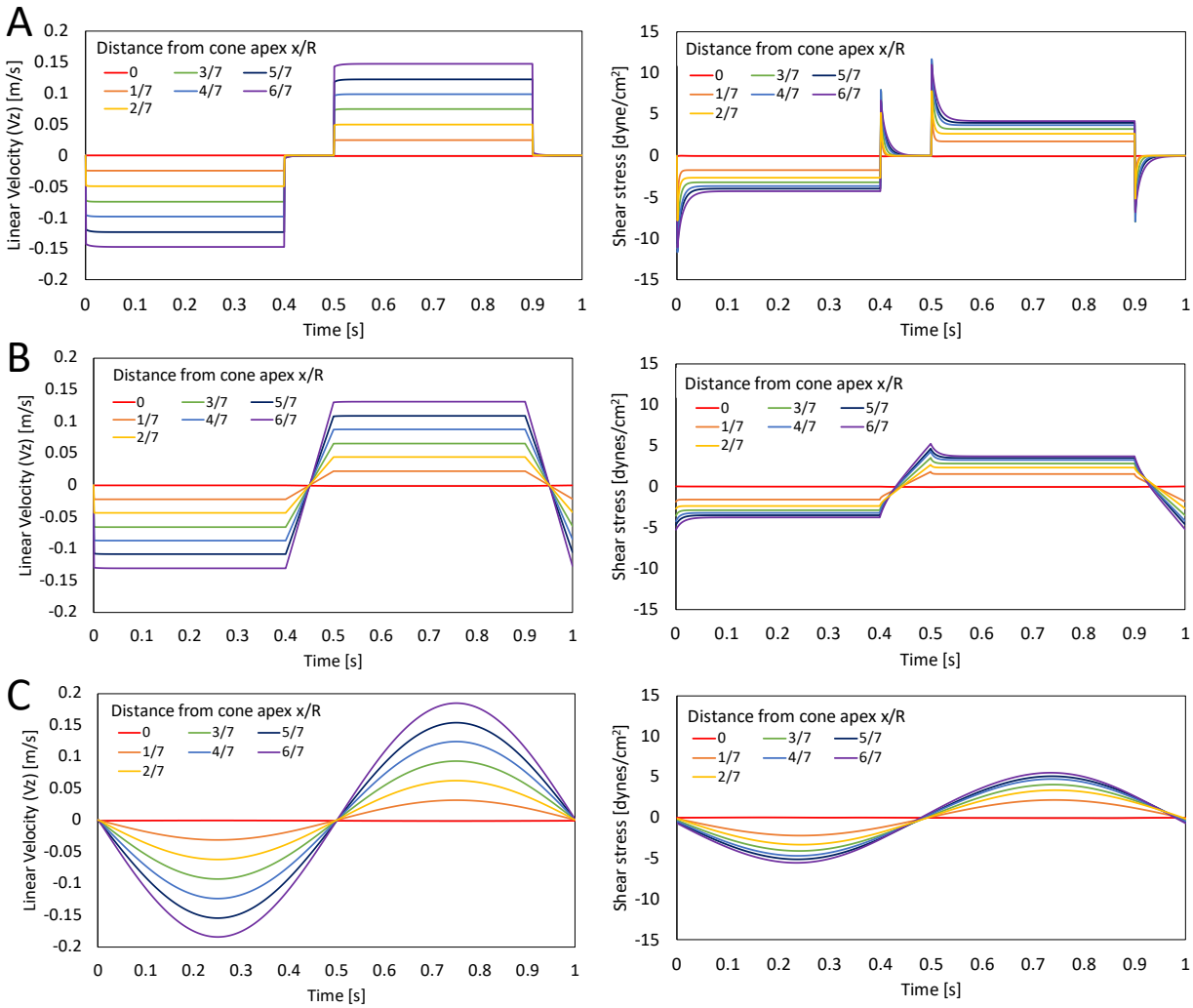

Figure 31: Velocity (left) and shear stress (right) profiles of oscillatory cases in a CPD. 1 period of rotation shown. Profiles shown as functions of time with relative distance from the cone apex (x/R) as a parameter. R = cone radius; 7.0 mm. A) Abruptly oscillating case. B) Oscillation with ramped acceleration. C) Sinusoidal oscillation. Velocity profiles given in linear velocities rather than angular because that is how the computational results were pulled from Fluent; $v_z = \omega * x$.

The shear stress profiles are qualitatively similar to those seen in the corresponding cases in the parallel plate geometry, which is a good indication that the simulation is being run correctly. The maximum and average shear stresses for each case are summarized in the table below.

Table 10: Shear stress summary statistics for the three oscillatory cases in a CPD. Maximum and average shear stresses [dyne/cm^2] reported. The shear stress is averaged over both position and time for each case.

Case Type	Maximum Shear Stress [dyne/cm^2]	Average Shear Stress [dyne/cm^2]
Abrupt	14.6	2.8
Ramped	9.94	2.7
Sinusoidal	10.2	2.7

While all three cases experience nearly identical average shear stresses along the cone length, there are differences in their maximums. The maximum shear stresses in the ramped and sinusoidal cases are very similar (percent difference < 3%), but there is a nearly 50% increase in when moving from the ramped or sinusoidal case to the abrupt case.

These results have implications for modeling flow through an actual aortic valve. If the valve's motion is more like the ramped or sinusoidal cases, the precise details of how the boundary conditions are modeled may not be as significant since such similar profiles are produced. However, if the aortic valve's motion is more abrupt, spikes in shear stress will be generated from the valve's motion that would not be captured by modeling the motion with a smoother velocity profile, making precise modeling much more important.

4.2.1. Shear Stress throughout cone volume

While shear stress in the CPD varies as you move radially outwards, it also changes as you move vertically within the volume between the cone and plate. Shear stress is highest closest to the cone, decreasing as you approach the plate. It is important to characterize this trend to know how much of the fluid experiences elevated levels of shear stress.

To test this, data were collected for each of the three cases (abrupt, ramped, and sinusoidal oscillation of the CPD) along the entire distance from plate to cone at a point 5 mm away from the

cone apex (x/R = 0.7). The shear stress was calculated at 11 evenly spaced points between the plate and cone over the course of the one second period for each case. Results are plotted below.

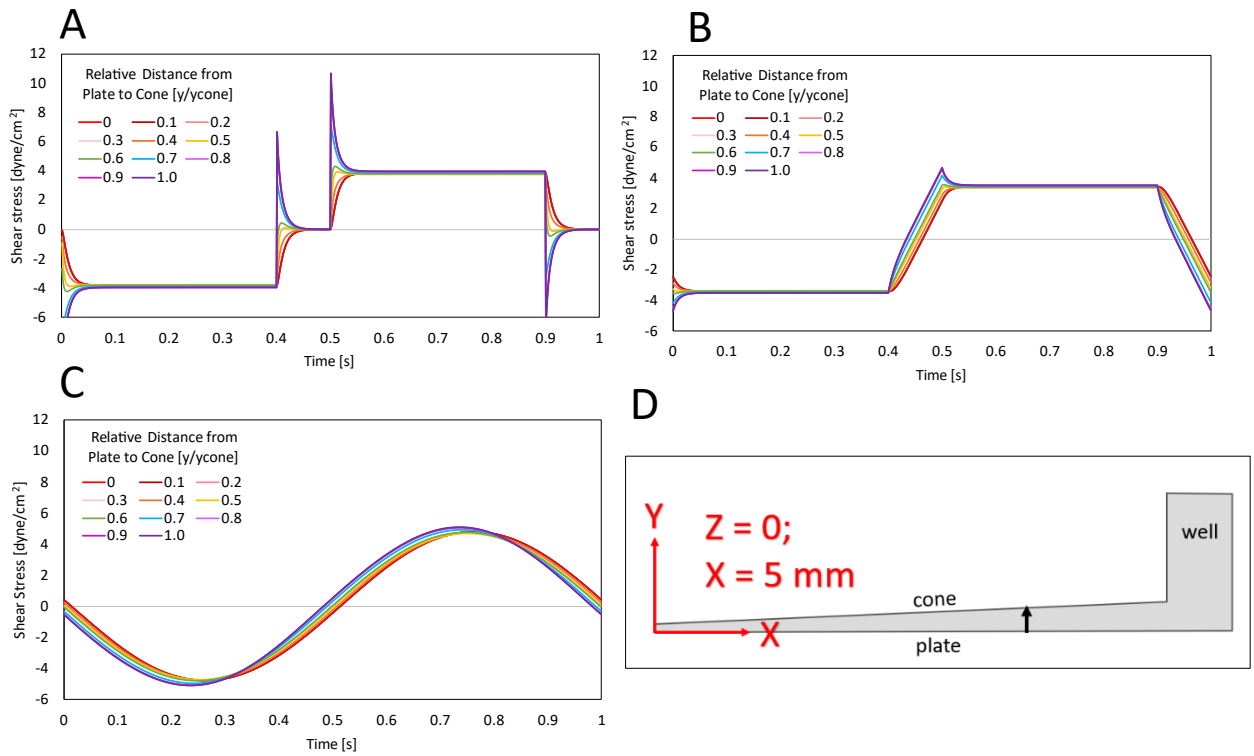

Figure 32: Shear stresses over time at positions between the cone and the plate. A) Abrupt stopping case. B) Ramped acceleration case. C) Sinusoidal oscillation case. D) Cross-section of cone taken at Z = 0 indicating where in the geometry the data were taken (X = 5 mm; Y from 0 to 0.318 mm).

Shear stress is higher closer to the cone in all cases, but this effect is most pronounced in the abrupt case (Fig. 32A), particularly where there are spikes in the shear stress. To better understand this effect, we can look at the maximum shear stress, rather than the shear stress over the entire period of oscillation. The figure below shows the peak shear stresses at points between the cone and plate, as a function of dimensionless position.

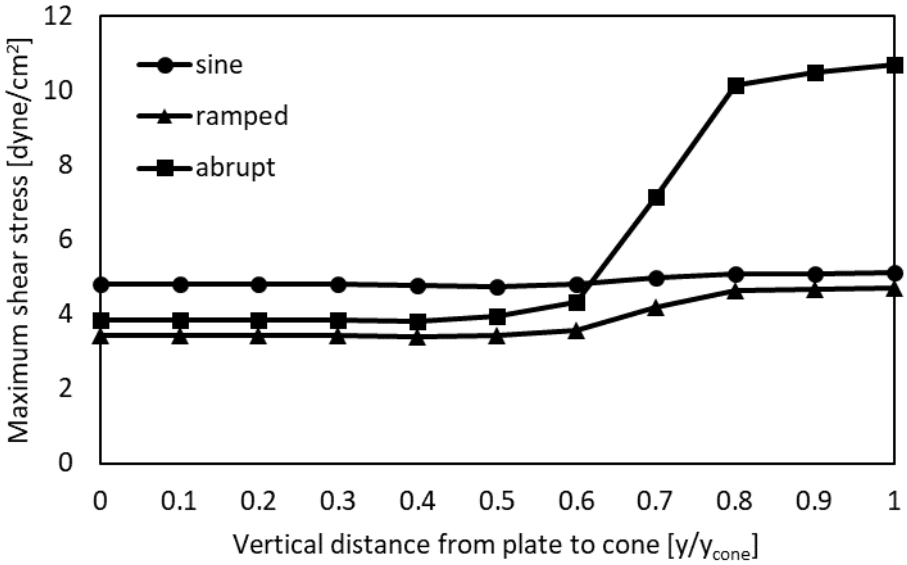

Figure 33: Maximum shear stresses in the fluid as a function of position between the plate and cone. On the X axis, 0 is the shear stress on the plate, and 1 is the shear stress on the cone. Maximum values found over the entire 1 second period of oscillation in each case.

The highest maximum shear stress for all cases occurs at the cone. For the abrupt case, this is 10.7 dyne/cm^2, which is much higher than both the ramped (4.72 dyne/cm^2) and sinusoidal (5.11 dyne/cm^2) cases. However, the *average* shear stress over the period changes little with either position or case type: for each case, the time and position-averaged maximum shear stresses are 3.18, 3.12, and 3.11 dyne/cm^2 for the abrupt, ramped, and sinusoidal cases, respectively.

In sum, the abrupt case has a much higher maximum shear stress than the ramped and sinusoidal cases, a finding that is relevant for the 30% of the fluid domain that experiences shear stresses above the average maximum between the cone and plate. Across all three cases, the average shear stress changes little across both time and position between the cone and plate. Therefore, if TGF-β activation is higher in the abrupt than in the ramped or sinusoidal cases, we know that it is that region of fluid where the peak shear stresses are highest where the TGF-β activation is occurring.

4.2.2 Shear Stress in the well

Next, the shear stress in the outer edge of the CPD was studied. The well, between the edge of the cone and the far wall, ranges from X = 7.0 mm to X = 7.9 mm. The shear stress at Y = 1.5 mm was studied as a function of position in the X direction and time. Results for each case (abrupt, ramped, and sinusoidal oscillation of the cone) are shown below.

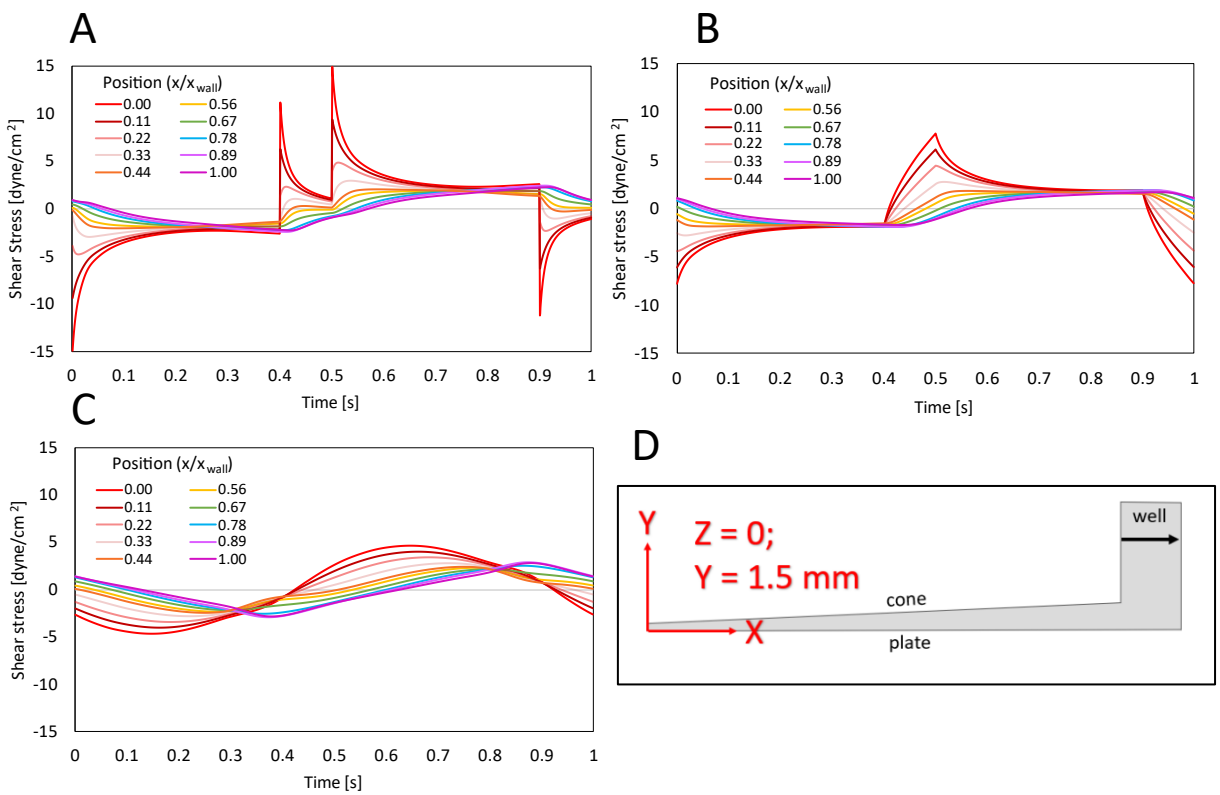

Figure 34: Shear stress as a function of time in the well past the edge of the cone. Dimensionless position calculated as X/X_{wall}, where 0 is at the edge of the cone (X = 7.0 mm), and X_{wall} is the outer wall, at X = 7.9 mm. A) Abrupt case. B) Ramped case. C) Sinusoidal case. D) Cross-section of the CPD with a black arrow showing where the data were taken.

Shear stress is highest in all cases closest to the cone edge, which is the moving surface. To better understand this trend, we can look at the maximum shear stress at each position, rather than the shear stress over the entire period of oscillation. The figure below shows the peak shear stresses at points from the edge of the cone to the outer wall, as a function of dimensionless position.

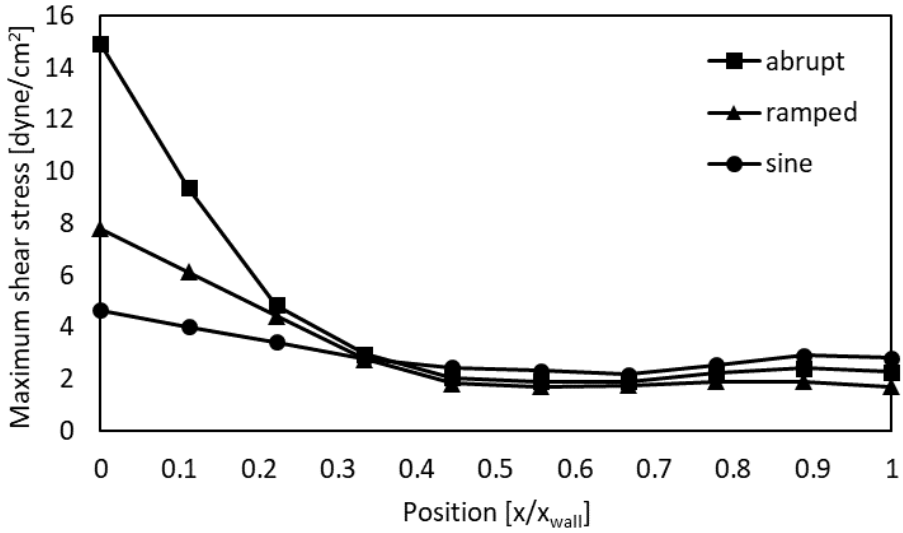

Figure 35: Maximum shear stresses in the fluid as a function of position in the well. On the X axis, 0 is the shear stress at the edge of the cone, and 1 is the shear stress on the outer wall. Maximum values found over the entire 1 second period of oscillation for each case.

The highest maximum shear stress for all cases occurs at the edge of the cone. For the abrupt case, this is 14.9 dyne/cm^2, which is much higher than both the ramped (7.79 dyne/cm^2) and sinusoidal (4.66 dyne/cm^2) cases. In all cases, about 20% of the fluid in the well experiences a maximum shear stress above the time and position-averaged maximum (4.49, 3.20, 3.01 dyne/cm^2 in the abrupt, ramped, and sinusoidal cases respectively).

In sum, we have looked at the maximum and time- and position-averaged shear stresses in a CPD and seen shear stress as a function of time, as well as position along the length of the spinning cone, between the cone and the plate, and in the well between the edge of the cone and the outer wall. In all cases, it is the fluid that is within the 30% of the volume closest to the cone in the region between the cone and plate and the 22% of the volume closest to the cone edge in the well, that experiences above average maximum shear stresses.

5. Discussion

This report focused on the differences between three different ways to generate oscillatory shear stress: through rotation with abrupt changes in direction, with linearly ramped acceleration/deceleration between direction changes, and sinusoidal oscillation. These cases were first modeled in Fluent in a parallel-plate geometry because its simplicity makes it easier to check that the results make logical sense. A plate gap of 1 mm was used in all cases and maximum velocities were on the order of 1 m/s, which is the average velocity of blood moving through the aortic valve[56]. All three cases had similar average shear stresses at the moving plate: 16.9, 15.1 and 15.3 dyne/cm^2 for the abrupt, ramped, and sinusoidal cases, respectively (abrupt and ramped cases with a 0.10 second stop/acceleration time). They did, however, have different maximum values: 175, 43,2, and 23.9 dyne/cm^2. A novel way of presenting the velocity and shear stress profiles was shown for each case that allows the viewer to see exactly what the velocity is at each point between the two plates for any given time.

The effect of changing the stop/acceleration time in the abrupt and ramped cases was studied, while keeping the 1 second cycle length constant. Stop times of 0.01, 0.05, and 0.10 s were tested and the maximum and average shear stresses compared. In the abrupt case, neither changed very much: maximum shear stresses at the plate were 169, 161, and 175 dyne/cm^2, respectively, with averages of 15.0, 15.8, and 16.9 dyne/cm^2. These differences could have some biological significance, if, say, a critical shear stress threshold was crossed between these values that would significantly increase TGF-β expression, but it is not likely. While the ramped case also had similar average shear stresses across the different times, much larger differences could be seen in the maximum values: 130, 60.2, and 43.2 dyne/cm^2 for acceleration times of 0.01, 0.05, and 0.10 seconds, respectively. As the stop time gets smaller, the ramped case shear stress profile

approaches that of the abrupt case. In the body, the mechanism of opening and closing the aortic valve likely falls somewhere between these two cases: not completely abrupt, but not simply linear acceleration. Studies have shown that valve closure occurs on the order of 10 msec[60], which makes the difference between the abrupt and ramped cases much less significant. However, the physical properties of the aortic valve change with disease progression, affecting the "close time" of the valve, further enforcing the importance of understanding how shear stress changes with different stop times.

Additionally, an analysis of the abrupt case over a wide range of Reynolds numbers (0.08-800) showed that while the peak shear stresses scale with Re, the profiles' behavior remains the same, even at very low Re. The fact that even very low inertial forces still produce strong spikes in shear stress is somewhat surprising, but what it means is that these trends remain applicable across a wide range of Re—they would not be affected by the variability in flowrates through the heart valves of different patients or different stages of stenosis, for example.

The three oscillatory profiles were then modeled with the geometry of a cone-and-plate device. The trends qualitatively aligned well with the findings in the parallel plate geometry, although quantitatively, calculated shear stresses were much lower because the simulations were run at lower velocities. In this case, it was found that 30% of the fluid between the cone and plate experiences elevated shear stresses (peak shear stresses above the position-averaged maximum), as does 20% of the fluid in the well.

6. Conclusions and Future Work

Prior research has shown that a) elevated levels of activated TGF-β are associated with the progression of calcific aortic valve disease[33], b) latent TGF-β is activated by fluid shear stress[27],

and c) as the aortic valve stenoses, it causes disturbances in the flow through the valve that are characterized by low, oscillatory velocity profiles[15]. Attempts have been made at imaging the stenotic heart valve in diseased patients, but it is difficult to precisely model the blood flow, and these models are heavily dependent on the patient's specific anatomy. Additionally, the exact mechanism through which TGF-β responds to shear stress is still unknown. Most experiments test the binary difference between shear and no shear, or steady and oscillatory shear. Modification of the shear stress environment or attenuation of TGF-β activation are potential pathways for treating CAVD, but for either of them to be effective, there needs to be a better understanding of the relationship between TGF-β activation and shear.

This report, through CFD simulation, demonstrates that even minute differences in how an oscillatory velocity profile is generated can create drastic differences in shear stress. When changes in direction happen abruptly, they generate spikes in shear stress that are not present when the changes in direction happen with linear acceleration.

The "disturbed flow" in literature is described as low, oscillatory flow. The three cases modeled in this report fit this description; however, the abrupt case sees large spikes in shear stress that are 5x higher than the average. Therefore, if TGF-β activation is higher in the abrupt case, we know that it is not necessarily the "low, oscillatory" nature of pathological shear stress that causes TGF-β activation, but transient spikes in shear stress that occur in narrow regions in the fluid. A way to test this would be to take samples from different parts of the fluid in the CPD (e.g. close to the cone where shear stress is high and further from the cone where the shear stress stays lower) and see if there are different levels of TGF-β activation in these different regions in the fluid. This is outside the scope of this paper but suggests an interesting area for future research.

Thus, we have the question: how significant are these abrupt spikes in shear stress to the activation of latent TGF-β? Does TGF-β respond to any changes in shear stress, prolonged changes in shear stress, or abrupt spikes? This question is best answered by coupling the computational results in this thesis with experimental data, which can be done using the cone and plate device that was used in Kouzbari *et al.*[50] and reprogrammed with different oscillatory profiles (see 3.2.1.2 for profile description and validation).

6.1. CPD Experiments

To test the effect of different shear profiles on TGF-β activation, experiments should be performed following the methods described in Kouzbari *et al.*[50] Five cases should be tested: no shear (no rotation of the cone at all), steady, unidirectional rotation of the cone, and bidirectional rotation of the cone with abrupt changes in direction, with ramped acceleration/deceleration between changes in direction, and with sinusoidal oscillation. The no shear and steady shear cases should be used as controls to describe baseline TGF-β activation. Any difference in latent TGF-β activation between the steady and sinusoidal cases will show the difference between steady and oscillatory shear. Any difference in activation between the abrupt and ramped cases will show the effect of temporary spikes in shear stress—if activation is significantly increased from ramped to abrupt, we can be confident that more TGF-β activation is occurring in the narrow band of fluid just below the rotating cone, during the points in the period when cone motion has just been started or stopped. Differences between the ramped and sinusoidal cases would show that TGF-β is extremely sensitive to changes in boundary conditions, because those two cases have nearly identical shear stress averages and maximums.

7. Appendices

7.1. Arduino Code

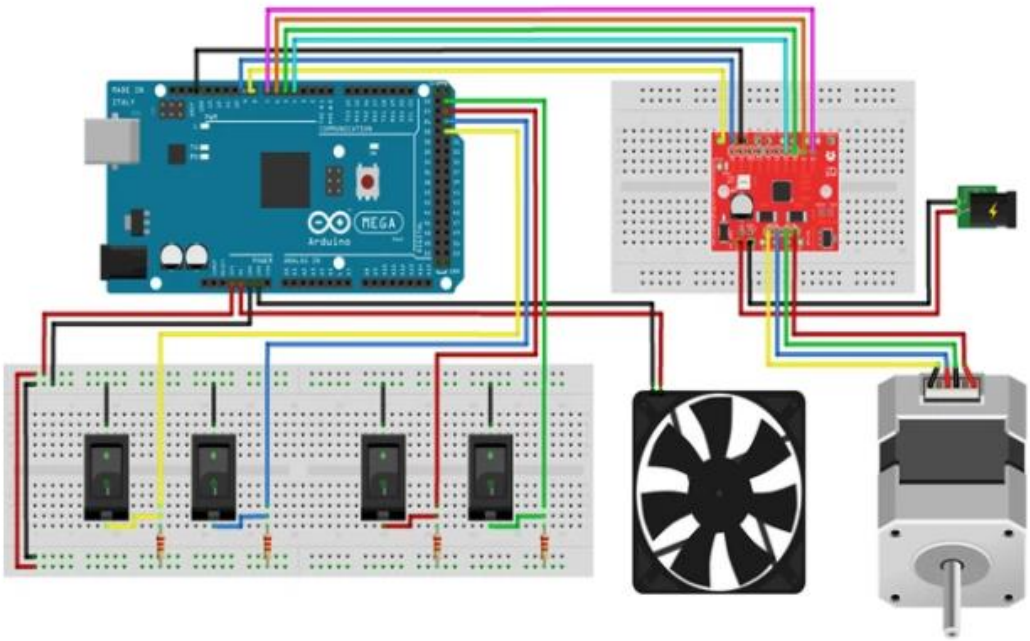

Figure 36: Wiring schematic of Arduino and Big Easy Driver for motor operation. Image from [50].

```
// Define Arduino Input Pins For Buttons
  // Buttons 1-4 labeled horizontally from top left
to bottom right
  const int Button1 = 11;    // Button 1 is attached
to Arduino pin 11
  const int Button2 = 26;    // Button 2 is attached
to Arduino pin 26
  const int Button3 = 10;    // Button 3 is attached
to Arduino pin 10
  const int Button4 = 24;    // Button 4 is attached
to Arduino pin 24
  int current_button = 0;    // determine which
button is pressed
  const int dirPin = 8;      // HIGH = CCW
rotation; LOW = CW rotation
  const int stepPin = 9;
  const int MS1 = 6;         // Big Easy Driver pins
for control of microstepping
  const int MS2 = 5;         // All 3 on HIGH is the
default; 1/16th step microstepping
  const int MS3 = 4;

// Arduino setup() function (REQUIRED)
void setup(){
  pinMode(Button1, INPUT_PULLUP);

  pinMode(Button2, INPUT_PULLUP);
  pinMode(Button3, INPUT_PULLUP);
  pinMode(Button4, INPUT_PULLUP);
  pinMode(dirPin, OUTPUT);
  pinMode(stepPin, OUTPUT);
  pinMode(MS1, OUTPUT);
  pinMode(MS2, OUTPUT);
  pinMode(MS3, OUTPUT);
} //close setup

// Arduino loop() function (REQUIRED)
void loop()
{
  // If Button 1 is pressed
  while(current_button == 1){
    continuousCase();     // put motor code in this
function below
```

```
    current_button =
ButtonNOW(Button1,Button2,Button3,Button4)
; // loop exit check: check to see if Button 1 is
still on
  }            // end while loop button 1

  // If Button 2 is pressed
  while(current_button == 2){
    abruptCase();       // put motor code in this
function below
    current_button =
ButtonNOW(Button1,Button2,Button3,Button4)
; // loop exit check: check to see if Button 2 is
still on
  }            // end while loop button 2

  // If Button 3 is pressed
  while(current_button == 3){
    rampedCase();     // put motor code in this
function below
    current_button =
ButtonNOW(Button1,Button2,Button3,Button4)
; // loop exit check: check to see if Button 3 is
still on
  }            // end while loop button 3

  // If Button 4 is pressed
  while(current_button == 4){
    sineCase();     // put motor code in this
function below
    current_button =
ButtonNOW(Button1,Button2,Button3,Button4)
; // loop exit check: check to see if Button 4 is
still on
  }            // end while loop button 4

  // If no button is pressed
  while(current_button == 0){
    noButtonCase();     // put motor code in this
function below
    current_button =
ButtonNOW(Button1,Button2,Button3,Button4)
; // loop exit check: check to see if all buttons are
still off
  }            // end while loop button 0
}              // end void loop

// RPM to microseconds calculations
  //The following 4 functions return the
necessary t_delay in microseconds to drive the
motor at a given RPM
  //RPM = (1 microstep / 2 t_delay)/(200
steps/rev)/(16 microsteps/step)*(1E6 us/sec)*(60
sec/min)
  //This calculation gives t_delay = 9375/RPM -
t_other for 16 microsteps/step. t_other is the
"think time" the code takes to execute, and is
different for each case.
  //1/8th microstepping mode gives t_delay =
18750/RPM - t_other
, and
  int ConstantmicroSeconds(int RPM) { //Use
this for the CONSTANT case with default
(1/16th) microstepping
      float t_delay = 9375/RPM -35.7;
      t_delay = round(t_delay);
      if(t_delay < 2.0){ // This is a safety check to
ensure the motor does not try to spin faster than
it can. A delay of 2 us should be about 250
RPM.
        t_delay = 2.0;
      } // end if statement
      if(t_delay > 900.0){ // This is a safety check
to ensure the motor does not try to spin slower
than is reasonable. A delay of 900 us should be
about 10 RPM.
        t_delay = 900.0;
      } // end if statement
      return (int)t_delay;
  }//end Constantmicroseconds function

   int AbruptmicroSeconds(int RPM) { //Use this
for the ABRUPT case with default (1/16th)
microstepping
      float t_delay = 18750/RPM - 10.6;
      t_delay = round(t_delay);
      if(t_delay < 20.0){ // This is a safety check
to ensure the motor does not try to spin faster
than is reasonable. A delay of 20 us should be
about 300 RPM.
        t_delay = 20.0;
      } // end if statement
      if(t_delay > 900.0){ // This is a safety check
to ensure the motor does not try to spin slower
than is reasonable. A delay of 900 us should be
about 10 RPM.
        t_delay = 900.0;
      } // end if statement
      return (int)t_delay;
  }//end Abruptmicroseconds function
```

```
  int RampedmicroSeconds(int RPM) { //Use
this for the RAMPED case with 1/8th
microstepping
    float t_delay = 18750/RPM - 10.6;
    t_delay = round(t_delay);
    if(t_delay < 50.0){ // This is a safety check
to ensure the motor does not try to spin faster
than is reasonable. A delay of 50 us should be
about 310 RPM.
      t_delay = 50.0;
    } // end if statement
    if(t_delay > 900.0){ // This is a safety check
to ensure the motor does not try to spin slower
than is reasonable. A delay of 900 us should be
about 20 RPM.
      t_delay = 900.0;
    } // end if statement
    return (int)t_delay;
  }//end Rampedmicroseconds function

  int SinemicroSeconds(int RPM) { //Use this for
the SINE case with 1/8th microstepping
    float t_delay = 18750/RPM - 48.9;
    t_delay = round(t_delay);
    if(t_delay < 8.0){ // This is a safety check to
ensure the motor does not try to spin faster than
is reasonable. A delay of 8 us should be about
330 RPM.
      t_delay = 8.0;
    } // end if statement
    if(t_delay > 900.0){ // This is a safety check
to ensure the motor does not try to spin slower
than is reasonable. A delay of 900 us should be
about 20 RPM.
      t_delay = 900.0;
    } // end if statement
    return (int)t_delay;
  }//end Sinemicroseconds function


// ButtonNOW function to determine which
button is currently on (if any)
int ButtonNOW(int button1, int button2, int
button3, int button4){
  int button_now1 = digitalRead(button1);
  int button_now2 = digitalRead(button2);
  int button_now3 = digitalRead(button3);
  int button_now4 = digitalRead(button4);
  if(button_now1 == LOW && button_now2 ==
HIGH && button_now3 == HIGH &&
button_now4 == HIGH){
    current_button = 1;
  }
  else if(button_now1 == HIGH &&
button_now2 == LOW && button_now3 ==
HIGH && button_now4 == HIGH){
    current_button = 2;
  }
  else if(button_now1 == HIGH &&
button_now2 == HIGH && button_now3 ==
LOW && button_now4 == HIGH){
    current_button = 3;
  }
  else if(button_now1 == HIGH &&
button_now2 == HIGH && button_now3 ==
HIGH && button_now4 == LOW){
    current_button = 4;
  }
  else{
    current_button = 0;   // this case is true if all
buttons are off OR if more than one button is on
  }
  return current_button;
}

// Code for continuous rotation of the motor
void continuousCase(){
    //continuous case variables
        const int rpm = 190;  //set the motor speed
        const int t_delay =
ConstantmicroSeconds(rpm);
    //continuous case setup
        digitalWrite(dirPin, HIGH); // HIGH =
CCW rotation
        digitalWrite(stepPin, LOW);
        digitalWrite(MS1, HIGH);    // 1/16th
microstepping
        digitalWrite(MS2, HIGH);
        digitalWrite(MS3, HIGH);
   //continuous case loop
        digitalWrite(stepPin, HIGH);
        delayMicroseconds(t_delay);
        digitalWrite(stepPin, LOW);
        delayMicroseconds(t_delay);
} // Close continuousCase

// Code for abrupt rotational changes for the
motor
void abruptCase(){
```

```
    //abrupt case variables
        const int rpmAbrupt = 240; //set the
motor speed
        const int t_delay =
AbruptmicroSeconds(rpmAbrupt);
        long t0 = millis();  // long data type
allows for 597 hours of operation (vs 30 seconds
with int data type)
        float t_hold = 0.4; //time (sec) to rotate
the motor in one direction
    //abrupt case setup
        digitalWrite(stepPin, LOW);
        digitalWrite(MS1, HIGH);  // 1/8th
microstepping
        digitalWrite(MS2, HIGH);
        digitalWrite(MS3, LOW);
    //abrupt case loop
        digitalWrite(dirPin, HIGH); // set
direction_pin to HIGH for counter-clockwise
(CCW) rotation
        t0 = millis(); // get current time before
starting next loop
        while(millis()-t0 < t_hold * 1000){ //
rotate motor 0.4 seconds in one direction
          delayMicroseconds(t_delay);
          digitalWrite(stepPin, HIGH);
          delayMicroseconds(t_delay);
          digitalWrite(stepPin, LOW);
          //delayMicroseconds(t_delay);
        }
        delay(100); // 100 ms delay
        t0 = millis(); // get current time before
starting next loop
        digitalWrite(dirPin, LOW); // set
direction_pin to LOW for clockwise (CW)
rotation
        while(millis()-t0 < t_hold * 1000){ //
rotate motor 0.4 seconds in the other direction
          digitalWrite(stepPin, HIGH);
          delayMicroseconds(t_delay);
          digitalWrite(stepPin, LOW);
          delayMicroseconds(t_delay);
        }
        delay(100); // 100 ms delay
} //Close abruptCase

// Code for oscillation of motor with ramped
acceleration/deceleration
void rampedCase(){
    //ramped case variables
        long t0 = millis();          //allows time-
based code to execute repeatedly
        const int rpm_max = 212;       //set the
maximum motor speed in RPMs
        const int rpm_min = -rpm_max;
//minimum motor speed in RPMs
        int rpm0 = 0;                //used in the
calculation RPM = RPM0 + a*t
        int t_delay = 0;             //in
microseconds, this controls the motor speed and
is calculated in the Microseconds function
        int rpm = 0;                 //working
motor speed in RPMs
        const float a = 4240;        //
acceleration (RPM/s). Calculated such that at
rpm_max = 212, acceleration time is 0.1 s
        int counter = 0;             //used to keep
the code from executing too often and slowing
down
    //ramped case setup
        int t_delay_max =
RampedmicroSeconds(rpm_max);
        int t_delay_min = t_delay_max;
        float t_hold = 0.4; // seconds to keep the
motor at its max/min speeds
        digitalWrite(stepPin, LOW);
        digitalWrite(MS1, HIGH); // 1/8th
microstepping
        digitalWrite(MS2, HIGH);
        digitalWrite(MS3, LOW);
    //ramped case loop
        digitalWrite(dirPin, HIGH); // HIGH =
CCW spinning
        t0 = millis();
        while(rpm < rpm_max) { //
ACCELERATE FROM 0 TO RPM_MAX
          while(counter < 8){ // this helps the
motor run smoother
            t_delay = RampedmicroSeconds(rpm);
            digitalWrite(stepPin, HIGH); // Start
taking a step
            delayMicroseconds(t_delay);
            digitalWrite(stepPin, LOW);
            delayMicroseconds(t_delay); // Finish
taking a step
            counter++;
          }
          rpm = rpm0 + a*(millis()-t0)/1000;
          counter = 0;
        } // ends while statement
        rpm = rpm_max;
```

```
        t_delay = t_delay_max;
        t0 = millis();
        while(millis()-t0  < t_hold*1000) { //
STAY AT RPM_MAX FOR T_HOLD
          digitalWrite(stepPin, HIGH); // Start
taking a step
          delayMicroseconds(t_delay);
          digitalWrite(stepPin, LOW);
          delayMicroseconds(t_delay); // Finish
taking a step
        } // ends if statement
        rpm0 = rpm_max;
        t0 = millis();
        while(rpm > 0) { // DECELERATE TO 0
RPM
          while(counter < 8){
            t_delay = RampedmicroSeconds(rpm);
            digitalWrite(stepPin, HIGH); // Start
taking a step
            delayMicroseconds(t_delay);
            digitalWrite(stepPin, LOW);
            delayMicroseconds(t_delay); // Finish
taking a step
            counter++;
          }
          rpm = rpm0 - a*(millis()-t0)/1000;
          counter = 0;
        } // ends if statement
        digitalWrite(dirPin, LOW); //LOW =
CW spinning; the dirPin switch is the reason the
acceleration/deceleration phases each need to be
in 2 parts
        rpm0 = 0;
        rpm = 0;
        t0 = millis();
        while(0 >= rpm && rpm > rpm_min) { //
DECELERATE TO RPM_MIN
          while(counter < 8){
            t_delay = RampedmicroSeconds(-
1*rpm);
            digitalWrite(stepPin, HIGH); // Start
taking a step
            delayMicroseconds(t_delay);
            digitalWrite(stepPin, LOW);
            delayMicroseconds(t_delay); // Finish
taking a step
            counter++;
          }
          rpm = rpm0 - a*(millis()-t0)/1000;
          counter = 0;
        } // ends if statement
        rpm = rpm_min;
        t_delay = t_delay_max;
        t0 = millis();
        while(millis()-t0  < t_hold*1000) { //
STAY AT RPM_MIN FOR T_HOLD
          digitalWrite(stepPin, HIGH); // Start
taking a step
          delayMicroseconds(t_delay);
          digitalWrite(stepPin, LOW);
          delayMicroseconds(t_delay); // Finish
taking a step
        } // ends if statement
        rpm0 = rpm_min;
        t0 = millis();
        while(rpm < 0) { // ACCELERATE TO
0 RPM
          while(counter < 8){
            t_delay = RampedmicroSeconds(-
1*rpm);
            digitalWrite(stepPin, HIGH); // Start
taking a step
            delayMicroseconds(t_delay);
            digitalWrite(stepPin, LOW);
            delayMicroseconds(t_delay); // Finish
taking a step
            counter++;
          }
          rpm = rpm0 + a*(millis()-t0)/1000;
          counter = 0;
        }
        //rpm0 = 0;
        //rpm = 0;
}//close rampedCase

// Code for sine wave oscillation of motor
void sineCase(){
    //sine case variables
        long t0 = millis();             //allows time-
based code to execute repeatedly
        int t_delay = 1;                //in
microseconds, this controls the motor speed and
is calculated in the Microseconds function
        int rpm = 1E-03;                //working
motor speed in RPMs
        int counter = 0;                //used to keep
the code from executing too often and slowing
down
        float two_pi = 2*3.14159;
        int a = 300;                    // RPM =
a*sin(b*t); a is in RPMs. This controls the max
speed of this function
```

```
        float b = 2*3.14159;            //RPM =
a*sin(b*t); b is in seconds
        float t_period = two_pi/b*1000;
//period of the sine curve in milliseconds
        boolean accelerate = true;       // true is
the 1st half of the sine curve; false is the 2nd
half
    //sine case setup
        digitalWrite(stepPin, LOW);
        digitalWrite(MS1, HIGH); // 1/8th
microstepping
        digitalWrite(MS2, HIGH);
        digitalWrite(MS3, LOW);
    //sine case loop
        digitalWrite(dirPin, HIGH); // HIGH =
CCW spinning
        t0 = millis();
        accelerate = true;
        while(accelerate == true && millis()-t0
< t_period/2 ) {  //FIRST HALF OF THE SINE
CURVE
          while(rpm > 0 && counter < 8){ // this
helps the motor run smoother
            t_delay = SinemicroSeconds(rpm);
            digitalWrite(stepPin, HIGH); // Start
taking a step
            delayMicroseconds(t_delay);
            digitalWrite(stepPin, LOW);
            delayMicroseconds(t_delay); // Finish
taking a step
            counter++;
          } //ends counter while
          rpm = a*sin(b*(millis()-t0)/1000);
          counter = 0;
        } // ends first half while statement
        accelerate = false;
        digitalWrite(dirPin, LOW); //LOW =
CW spinning
        t0 = millis();
        rpm = 1E-03;
          while(accelerate == false && millis()-
t0 < t_period/2) { //SECOND HALF OF THE
SINE CURVE
            while(rpm > 0 && counter < 8){
              t_delay = SinemicroSeconds(rpm);
              digitalWrite(stepPin, HIGH); // Start
taking a step
              delayMicroseconds(t_delay);
              digitalWrite(stepPin, LOW);
              delayMicroseconds(t_delay); //
Finish taking a step
              counter++;
            } //ends counter while
            rpm = a*sin(b*(millis()-t0)/1000);
            counter = 0;
          } // ends second half while statement
        accelerate = true;
        t0 = millis();
        rpm = 1E-03;
}//close sineCase

// Code for when no button is pressed
void noButtonCase(){
  digitalWrite(stepPin, LOW);
}//close noButtonCase
```

7.2. Alternative figures

The following figures reflect an alternative way to depict the data shown in 4.1.4. These graphs group together data based on case type, instead of stop time. Velocity and shear stress profiles for the abrupt and ramped cases at three different stop/acceleration times shown.

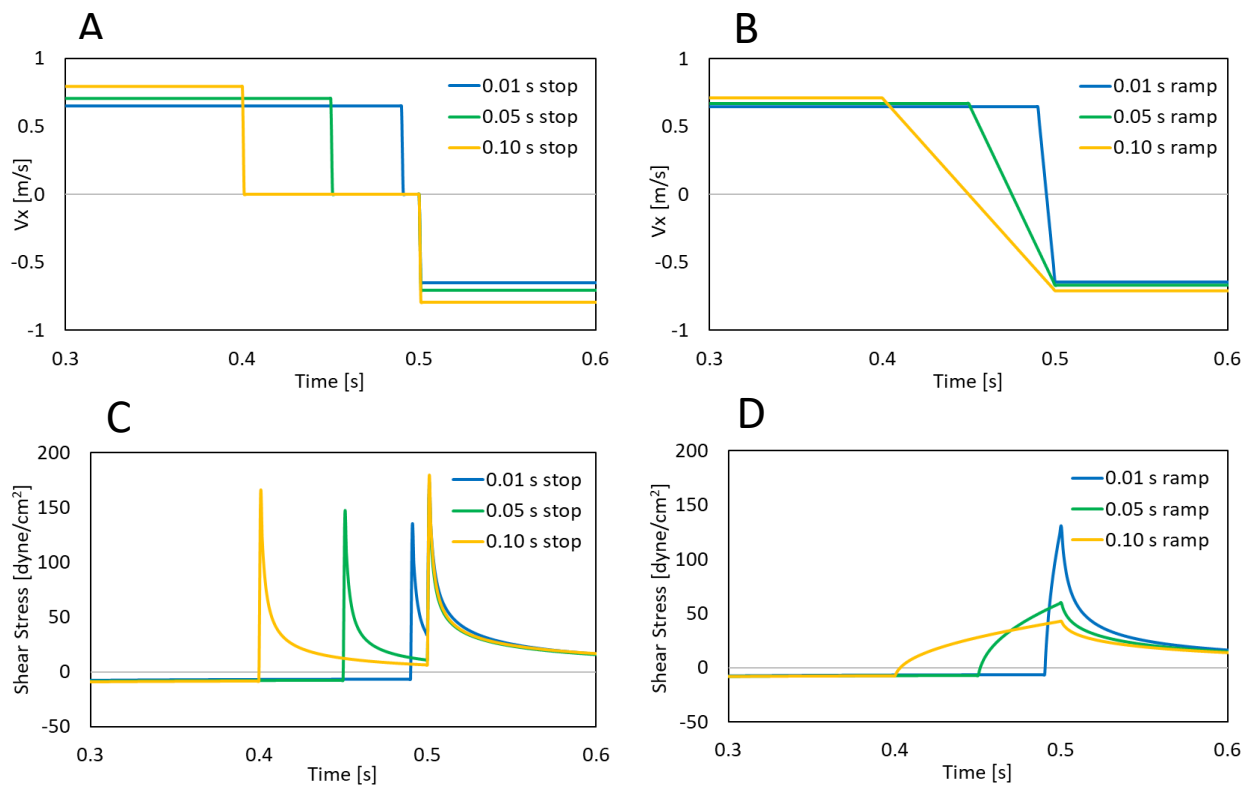

Figure 37: Velocity and shear stresses for the abrupt stopping and ramped acceleration cases for different stop times. A) Velocity profiles for the abrupt cases. B) Velocity profiles for the ramped cases. C) Shear stress profiles for the abrupt cases. D) Shear stress profiles for the ramped cases. In all figures, the three different stop/acceleration periods are 0.01 s (blue line), 0.05 s (green line), and 0.10 s (yellow line).

8. References

1. Yutzey, K. E., Demer, L. L., Body, S. C., Huggins, G. S., Towler, D. A., Giachelli, C. M., . . . Aikawa, E. (2014). Calcific Aortic Valve Disease. *Arteriosclerosis, Thrombosis, and Vascular Biology, 34*(11), 2387-2393. doi:doi:10.1161/ATVBAHA.114.302523
2. Virani, S. S., Alonso, A., Aparicio, H. J., Benjamin, E. J., Bittencourt, M. S., Callaway, C. W., . . . Stroke Statistics, S. (2021). Heart Disease and Stroke Statistics-2021 Update: A Report From the American Heart Association. *Circulation*, CIR0000000000000950. doi:10.1161/CIR.0000000000000950
3. Lerman, D. A., Prasad, S., & Alotti, N. (2015). Calcific Aortic Valve Disease: Molecular Mechanisms and Therapeutic Approaches. *Eur Cardiol, 10*(2), 108-112. doi:10.15420/ecr.2015.10.2.108
4. Otto, C. M. (2008). Calcific Aortic Stenosis — Time to Look More Closely at the Valve. *New England Journal of Medicine, 359*(13), 1395-1398. doi:10.1056/NEJMe0807001
5. Walshe, T. E., Paz, N. G. d., & D'Amore, P. A. (2013). The Role of Shear-Induced Transforming Growth Factor-β Signaling in the Endothelium. *Arteriosclerosis, Thrombosis, and Vascular Biology, 33*(11), 2608-2617. doi:doi:10.1161/ATVBAHA.113.302161
6. Ohno, M., Cooke, J. P., Dzau, V. J., & Gibbons, G. H. (1995). Fluid shear stress induces endothelial transforming growth factor beta-1 transcription and production. Modulation by potassium channel blockade. *The Journal of Clinical Investigation, 95*(3), 1363-1369. doi:10.1172/JCI117787
7. Merryman, W. D., & Schoen, F. J. (2013). Mechanisms of calcification in aortic valve disease: role of mechanokinetics and mechanodynamics. *Curr Cardiol Rep, 15*(5), 355. doi:10.1007/s11886-013-0355-5
8. Rajamannan, N. M., Evans, F. J., Aikawa, E., Grande-Allen, K. J., Demer, L. L., Heistad, D. D., . . . Otto, C. M. (2011). Calcific aortic valve disease: not simply a degenerative process: A review and agenda for research from the National Heart and Lung and Blood Institute Aortic Stenosis Working Group. Executive summary: Calcific aortic valve disease-2011 update. *Circulation, 124*(16), 1783-1791. doi:10.1161/circulationaha.110.006767
9. Liu, A. C., Joag, V. R., & Gotlieb, A. I. (2007). The emerging role of valve interstitial cell phenotypes in regulating heart valve pathobiology. *Am J Pathol, 171*(5), 1407-1418. doi:10.2353/ajpath.2007.070251
10. O'Brien, K. D. (2006). Pathogenesis of Calcific Aortic Valve Disease. *Arteriosclerosis, Thrombosis, and Vascular Biology, 26*(8), 1721-1728. doi:doi:10.1161/01.ATV.0000227513.13697.ac
11. Pedriali, G., Morciano, G., Patergnani, S., Cimaglia, P., Morelli, C., Mikus, E., . . . Pinton, P. (2020). Aortic Valve Stenosis and Mitochondrial Dysfunctions: Clinical and Molecular Perspectives. *International Journal of Molecular Sciences, 21*(14), 4899. Retrieved from https://www.mdpi.com/1422-0067/21/14/4899
12. Bird, R. B., Stewart, W. E., & Lightfoot, E. N. (2006). *Transport phenomena* (Vol. 1): John Wiley & Sons.
13. Durairaj, K., Vinoth, R., Raviraj, A., & Shankar, C. S. (2017). Non-Newtonian and newtonian blood flow in human aorta: A transient analysis. *Biomedical Research (India), 28*, 3194-3203.

14. Cunningham, K. S., & Gotlieb, A. I. (2005). The role of shear stress in the pathogenesis of atherosclerosis. *Laboratory Investigation, 85*(1), 9-23. doi:10.1038/labinvest.3700215
15. Simmons, C. A., Grant, G. R., Manduchi, E., & Davies, P. F. (2005). Spatial heterogeneity of endothelial phenotypes correlates with side-specific vulnerability to calcification in normal porcine aortic valves. *Circulation research, 96*(7), 792-799. doi:10.1161/01.RES.0000161998.92009.64
16. Butcher, J. T., Tressel, S., Johnson, T., Turner, D., Sorescu, G., Jo, H., & Nerem, R. M. (2006). Transcriptional Profiles of Valvular and Vascular Endothelial Cells Reveal Phenotypic Differences. *Arteriosclerosis, Thrombosis, and Vascular Biology, 26*(1), 69-77. doi:doi:10.1161/01.ATV.0000196624.70507.0d
17. Jenkins, N. T., Padilla, J., Boyle, L. J., Credeur, D. P., Laughlin, M. H., & Fadel, P. J. (2013). Disturbed blood flow acutely induces activation and apoptosis of the human vascular endothelium. *Hypertension (Dallas, Tex. : 1979), 61*(3), 615-621. doi:10.1161/HYPERTENSIONAHA.111.00561
18. Nicosia, M. A., Cochran, R. P., Einstein, D. R., Rutland, C. J., & Kunzelman, K. S. (2003). A coupled fluid-structure finite element model of the aortic valve and root. *J Heart Valve Dis, 12*(6), 781-789.
19. Sucosky, P., Balachandran, K., Elhammali, A., Jo, H., & Yoganathan, A. P. (2009). Altered shear stress stimulates upregulation of endothelial VCAM-1 and ICAM-1 in a BMP-4- and TGF-beta1-dependent pathway. *Arteriosclerosis, Thrombosis, and Vascular Biology, 29*(2), 254-260. doi:10.1161/ATVBAHA.108.176347
20. Chen, Y., & Ju, L. A. (2020). Biomechanical thrombosis: the dark side of force and dawn of mechano-medicine. *Stroke and Vascular Neurology, 5*(2), 185. doi:10.1136/svn-2019-000302
21. Sadler, J. E. (1998). Biochemistry and Genetics of Von Willebrand Factor. *Annual Review of Biochemistry, 67*(1), 395-424. doi:10.1146/annurev.biochem.67.1.395
22. Schneider, S. W., Nuschele, S., Wixforth, A., Gorzelanny, C., Alexander-Katz, A., Netz, R. R., & Schneider, M. F. (2007). Shear-induced unfolding triggers adhesion of von Willebrand factor fibers. *Proceedings of the National Academy of Sciences, 104*(19), 7899. doi:10.1073/pnas.0608422104
23. Fu, H., Jiang, Y., Yang, D., Scheiflinger, F., Wong, W. P., & Springer, T. A. (2017). Flow-induced elongation of von Willebrand factor precedes tension-dependent activation. *Nature Communications, 8*(1), 324. doi:10.1038/s41467-017-00230-2
24. Löf, A., Müller, J. P., & Brehm, M. A. (2018). A biophysical view on von Willebrand factor activation. *J Cell Physiol, 233*(2), 799-810. doi:10.1002/jcp.25887
25. Li, M. O., & Flavell, R. A. (2008). TGF-beta: a master of all T cell trades. *Cell, 134*(3), 392-404. doi:10.1016/j.cell.2008.07.025
26. Kubiczkova, L., Sedlarikova, L., Hajek, R., & Sevcikova, S. (2012). TGF-β – an excellent servant but a bad master. *Journal of Translational Medicine, 10*(1), 183. doi:10.1186/1479-5876-10-183
27. Ahamed, J., Burg, N., Yoshinaga, K., Janczak, C. A., Rifkin, D. B., & Coller, B. S. (2008). In vitro and in vivo evidence for shear-induced activation of latent transforming growth factor-β1. *Blood, 112*(9), 3650-3660. doi:10.1182/blood-2008-04-151753
28. Negishi, M., Lu, D., Zhang, Y.-Q., Sawada, Y., Sasaki, T., Kayo, T., . . . Takeuchi, T. (2001). Upregulatory Expression of Furin and Transforming Growth Factor Beta by Fluid Shear

Stress in Vascular Endothelial Cells. *Arteriosclerosis, Thrombosis, and Vascular Biology, 21*(5), 785-790. doi:doi:10.1161/01.ATV.21.5.785
29. Wang, W., Vootukuri, S., Meyer, A., Ahamed, J., & Coller, B. S. (2014). Association Between Shear Stress and Platelet-Derived Transforming Growth Factor Beta;1 Release and Activation in Animal Models of Aortic Valve Stenosis. *Arteriosclerosis, Thrombosis, and Vascular Biology, 34*(9), 1924-1932. doi:doi:10.1161/ATVBAHA.114.303852
30. Kunnen, S. J., Leonhard, W. N., Semeins, C., Hawinkels, L. J. A. C., Poelma, C., ten Dijke, P., . . . Peters, D. J. M. (2017). Fluid shear stress-induced TGF-β/ALK5 signaling in renal epithelial cells is modulated by MEK1/2. *Cellular and Molecular Life Sciences, 74*(12), 2283-2298. doi:10.1007/s00018-017-2460-x
31. Kapoor, R. (2018). *Investigating the mechanisms of renal fibrosis following ischaemia and reperfusion injury*.
32. Goody, P. R., Hosen, M. R., Christmann, D., Niepmann, S. T., Zietzer, A., Adam, M., . . . Jansen, F. (2020). Aortic Valve Stenosis: From Basic Mechanisms to Novel Therapeutic Targets. *Arterioscler Thromb Vasc Biol, 40*(4), 885-900. doi:10.1161/atvbaha.119.313067
33. Jian, B., Narula, N., Li, Q.-y., Mohler, E., & Levy, R. (2003). Progression of aortic valve stenosis: TGF-beta1 is present in calcified aortic valve cuSPS and promotes aortic valve interstitial cell calcification via apoptosis. *The Annals of thoracic surgery, 75*, 457-465; discussion 465. doi:10.1016/S0003-4975(02)04312-6
34. Varshney, R., Murphy, B., Woolington, S., Ghafoory, S., Chen, S., Robison, T., & Ahamed, J. (2019). Inactivation of platelet-derived TGF-β1 attenuates aortic stenosis progression in a robust murine model. *Blood advances, 3*(5), 777-788. doi:10.1182/bloodadvances.2018025817
35. Ong, C. W., Wee, I., Syn, N., Ng, S., Leo, H. L., Richards, A. M., & Choong, A. (2020). Computational Fluid Dynamics Modeling of Hemodynamic Parameters in the Human Diseased Aorta: A Systematic Review. *Ann Vasc Surg, 63*, 336-381. doi:10.1016/j.avsg.2019.04.032
36. Morris, P. D., Narracott, A., von Tengg-Kobligk, H., Silva Soto, D. A., Hsiao, S., Lungu, A., . . . Gunn, J. P. (2016). Computational fluid dynamics modelling in cardiovascular medicine. *Heart, 102*(1), 18. doi:10.1136/heartjnl-2015-308044
37. Razaghi, R., Biglari, H., & Karimi, A. (2019). Risk of rupture of the cerebral aneurysm in relation to traumatic brain injury using a patient-specific fluid-structure interaction model. *Computer Methods and Programs in Biomedicine, 176*, 9-16. doi:https://doi.org/10.1016/j.cmpb.2019.04.015
38. Sforza, D. M., Putman, C. M., & Cebral, J. R. (2012). Computational fluid dynamics in brain aneurysms. *International journal for numerical methods in biomedical engineering, 28*(6-7), 801-808. doi:10.1002/cnm.1481
39. Dwyer, H. A., Matthews, P. B., Azadani, A., Jaussaud, N., Ge, L., Guy, T. S., & Tseng, E. E. (2009). Computational fluid dynamics simulation of transcatheter aortic valve degeneration. *Interact Cardiovasc Thorac Surg, 9*(2), 301-308. doi:10.1510/icvts.2008.200006
40. Youssefi, P., Gomez, A., He, T., Anderson, L., Bunce, N., Sharma, R., . . . Jahangiri, M. (2017). Patient-specific computational fluid dynamics—assessment of aortic hemodynamics in a spectrum of aortic valve pathologies. *The Journal of Thoracic and Cardiovascular Surgery, 153*(1), 8-20.e23. doi:https://doi.org/10.1016/j.jtcvs.2016.09.040
41. Yap, C. H., Saikrishnan, N., Tamilselvan, G., & Yoganathan, A. P. (2012). Experimental measurement of dynamic fluid shear stress on the aortic surface of the aortic valve leaflet.

Biomechanics and Modeling in Mechanobiology, 11(1), 171-182. doi:10.1007/s10237-011-0301-7
42. Khe, A. K., Cherevko, A. A., Chupakhin, A. P., Bobkova, M. S., Krivoshapkin, A. L., & Orlov, K. Y. (2016, June 01, 2016). *Haemodynamics of giant cerebral aneurysm: A comparison between the rigid-wall, one-way and two-way FSI models*.
43. Makhijani, V. B., Yang, H. Q., Dionne, P. J., & Thubrikar, M. J. (1997). Three-dimensional coupled fluid-structure simulation of pericardial bioprosthetic aortic valve function. *Asaio j, 43*(5), M387-392.
44. Peskin, C. S., & McQueen, D. M. (1995). A general method for the computer simulation of biological systems interacting with fluids. *Symp Soc Exp Biol, 49*, 265-276.
45. Hoeijmakers, M. J. M. M., Silva Soto, D. A., Waechter-Stehle, I., Kasztelnik, M., Weese, J., Hose, D. R., & de Vosse, F. N. v. (2019). Estimation of valvular resistance of segmented aortic valves using computational fluid dynamics. *Journal of Biomechanics, 94*, 49-58. doi:https://doi.org/10.1016/j.jbiomech.2019.07.010
46. Grewal, N., & Gittenberger-de Groot, A. C. (2019). Wall Shear Stress Directional Abnormalities in BAV Aortas: Toward a New Hemodynamic Predictor of Aortopathy? *Frontiers in physiology, 10*, 225-225. doi:10.3389/fphys.2019.00225
47. Caballero, A. D., & Laín, S. (2013). A Review on Computational Fluid Dynamics Modelling in Human Thoracic Aorta. *Cardiovascular Engineering and Technology, 4*(2), 103-130. doi:10.1007/s13239-013-0146-6
48. Sucosky, P., Padala, M., Elhammali, A., Balachandran, K., Jo, H., & Yoganathan, A. P. (2008). Design of an ex vivo culture system to investigate the effects of shear stress on cardiovascular tissue. *J Biomech Eng, 130*(3), 035001. doi:10.1115/1.2907753
49. Breen, L., McHugh, P., McCormack, B., Muir, G., Quinlan, N., Heraty, K., & Murphy, B. (2006). Development of a novel bioreactor to apply shear stress and tensile strain simultaneously to cell monolayers. *Review of Scientific Instruments, 77*. doi:10.1063/1.2356857
50. Kouzbari, K., Hossan, M. R., Arrizabalaga, J. H., Varshney, R., Simmons, A. D., Gostynska, S., . . . Ahamed, J. (2019). Oscillatory shear potentiates latent TGF-β1 activation more than steady shear as demonstrated by a novel force generator. *Scientific Reports, 9*(1), 6065. doi:10.1038/s41598-019-42302-x
51. Buschmann, M. H., Dieterich, P., Adams, N. A., & Schnittler, H. J. (2005). Analysis of flow in a cone-and-plate apparatus with respect to spatial and temporal effects on endothelial cells. *Biotechnol Bioeng, 89*(5), 493-502. doi:10.1002/bit.20165
52. Spruell, C., & Baker, A. B. (2013). Analysis of a high-throughput cone-and-plate apparatus for the application of defined spatiotemporal flow to cultured cells. *Biotechnol Bioeng, 110*(6), 1782-1793. doi:10.1002/bit.24823
53. Franzoni, M., Cattaneo, I., Ene-Iordache, B., Oldani, A., Righettini, P., & Remuzzi, A. (2016). Design of a cone-and-plate device for controlled realistic shear stress stimulation on endothelial cell monolayers. *Cytotechnology, 68*(5), 1885-1896. doi:10.1007/s10616-015-9941-2
54. Ansys, F. I. (2012). Fluent theory guide.
55. Welty, J., Rorrer, G. L., & Foster, D. G. (2014). *Fundamentals of momentum, heat, and mass transfer*: John Wiley & Sons.

56. Chaothawee, L. (2012). Diagnostic approach to assessment of valvular heart disease using magnetic resonance imaging, part II: a practical approach for native and prosthetic heart valve stenosis. *Heart Asia, 4*(1), 171-175. doi:10.1136/heartasia-2012-010124
57. Sakariassen, K. S., Orning, L., & Turitto, V. T. (2015). The impact of blood shear rate on arterial thrombus formation. *Future science OA, 1*(4), FSO30-FSO30. doi:10.4155/fso.15.28
58. Butcher, J. T., & Nerem, R. M. (2007). Valvular endothelial cells and the mechanoregulation of valvular pathology. *Philosophical transactions of the Royal Society of London. Series B, Biological sciences, 362*(1484), 1445-1457. doi:10.1098/rstb.2007.2127
59. Leyh, R. G., Schmidtke, C., Sievers, H.-H., & Yacoub, M. H. (1999). Opening and Closing Characteristics of the Aortic Valve After Different Types of Valve-Preserving Surgery. *Circulation, 100*(21), 2153-2160. doi:doi:10.1161/01.CIR.100.21.2153
60. Anastassiades, P. C., Quinones, M. A., Gaasch, W. H., Adyanthaya, A. V., Waggoner, A. D., & Alexander, J. K. (1976). Aortic valve closure: Echocardiographic, phonocardiographic, and hemodynamic assessment. *American Heart Journal, 91*(2), 228-232. doi:https://doi.org/10.1016/S0002-8703(76)80578-9